LABVIEW IMPLEMENTATION OF THE ELECTROMECHANICAL IMPEDANCE (EMI) METHOD AS PART OF AN INTEGRATED STRUCTURAL HEALTH MONITORING (SHM) SYSTEM

by

Zhaoyun Ma

B.S., Wuhan University of Technology, 2012

M.S., Wuhan University of Technology, 2015

Submitted to the Graduate Faculty of

Swanson School of Engineering in partial fulfillment

of the requirements for the degree of

Master of Science

University of Pittsburgh

2016

UNIVERSITY OF PITTSBURGH

SWANSON SCHOOL OF ENGINEERING

This thesis was presented

by

Zhaoyun Ma

It was defended on

November 8, 2016

and approved by

Qiang Yu, Ph.D., Assistant Professor

Department of Civil & Environmental Engineering

Jeen-shang Lin, Ph.D., Associate Professor

Department of Civil & Environmental Engineering

Thesis Advisor: Piervincenzo Rizzo, Ph.D., Associate Professor

Department of Civil & Environmental Engineering

Copyright © by Zhaoyun Ma

2016

LABVIEW IMPLEMENTATION OF THE ELECTROMECHANICAL IMPEDANCE (EMI) METHOD AS PART OF AN INTEGRATED STRUCTURE HEALTH MONITORING (SHM) SYSTEM

Zhaoyun Ma, M.S.

University of Pittsburgh, 2016

There is an escalating interest in monitoring sensing system to assess the health of engineering structures in real-time. A wide body of literature demonstrated that structural health monitoring (SHM) methods based on acoustic emission (AE), electromechanical impedance (EMI), and guided ultrasonic waves (GUWs) can assess the health of simple waveguides and a certain number of complex structures. AE, EMI, and GUW have advantages and limitations. To boost the advantages and to overcome the shortcomings, a group at the University of Pittsburgh is working on a multi-modal integrated SHM where the three methods are driven by a single centralized hardware working under LabView environment. The suite mimics the sensory integration and processing of the human body, where the stimuli from the five sensory organs are transmitted by the nerves to the brain.

In this thesis, we present the integration of the EMI and the GUW-based methods in LabView and the analysis of the EMI data. A large flat aluminum plate was monitored with an array of six transducers and damage was simulated by adding small masses to the plate. Then, the GUW and AE waveforms were analyzed using a common statistical index. The results presented in this thesis show that the EMI enable the detection of the simulated damage.

TABLE OF CONTENTS

LIST OF TABLES

LIST OF FIGURES

ACKNOWLEDGEMENTS

I had an incredible experience during the one year and half graduate studies at Civil & Environmental Engineering Department at University of Pittsburgh. I would like to thank all the people who have helped me.

First, I would like to express my special gratitude to my Master adviser, Professor Piervincenzo Rizzo, for all the motivation, support and guidance during my graduate studies at University of Pittsburgh.

I would like to thank my Master thesis defense committee members, Professor Jeen-shang Lin and Professor Qiang Yu for supporting my research and providing me with helpful feedback in time, which significantly improves the quality of my work. I would like to thank the visiting scholar Vincenzo Gulizzi, for the detailed explanation of my questions about the experiment.

I would also like to thank all my amazing officemates and friends Kaiyuna Li, Wen Deng and Amir Nasrollahi. I appreciate all the code debugging, research discussion and practice presentation I had with each of you. Without their help, the project could not have been successfully conducted.

I must thank all my incredible friends, Yuwei, Raphael, Alen, Omkar and Natalia, who have stuck by me through thick and thin. Also, this graduate school journey would have been impossible without the support of my amazing parents Chunpo and Hua back in China. Finally, I want to extend big thanks to my best friends Tianqiao and Qi for always supporting me.

1.0 INTRODUCTION

In recent years, there has been an escalating attention to Structural Health Monitoring (SHM) systems to detect, locate and identify damage in a wide variety of engineering infrastructures. Existing infrastructures are prone to aging and deteriorations that may lead to the onset and growth of cracks, corrosion, etc. Periodic inspection is usually implemented in many civil and aerospace structures but this may still not prevent sudden failures between two inspection routines. To reduce the long-term cost of maintenance, online SHM systems are expected to be incorporated in new structures during the construction process or in existing structures that deserve special consideration. Hence, robust and efficient SHM systems able to monitor structures 24/7 should be developed and have caught the attention of many researchers and industries in the last two decades.

One of the main challenges in SHM is to obtain as much information as possible from the structures in real time. The nondestructive evaluation (NDE) methods typically implemented for SHM include Guided Ultrasonic Waves (GUWSs), Electromechanical Impedance (EMI), Acoustic Emission (AE), Modal Analysis etc., However, each method has its own advantages and limitations. Thus, it would be preferred to incorporate different NDE methods into a simple integrated SHM system that minimize the drawbacks of each method.

In this thesis, an integrated SHM system employing EMI and GUWs simultaneously is presented. In general, GUWs-based methods are implemented either by exciting narrowband tone bursts and capturing only a few control modes or by actuating broadband pulses and receiving all the modes. Lead zirconate titanate transducers (PZTs) can be used to generate and detect GUWs. The EMI approach exploits instead the relationship between the electrical impedance of a PZT and the mechanical impedance of the structure to which the PZT is bonded or embedded. A variation in the impedance signature of the PZT may indicate the presence of damage in the host structure. Thus, these two methods can be integrated in a SHM system by employing the same PZT.

In the work presented in this thesis, we develop LabVIEW program to drive an integrated GUW and EMI system implemented in a National Instruments PXIe 1062Q (NI PXI). The system is tested experimentally by using six PZT transducers bonded to an aluminum plate subject to simulated damage. The EMI data are processed using four damage metrics, and the results obtained from EMI analysis show that the array of PZTs can detect the simulated damage scenarios. The ultrasonic data are processed to create an image of the plate. As the data analysis of guided waves is not part of this thesis, results are not presented here.

This thesis is organized as follows. In chapter 2, the overall principle of the EMI method is described along with a state of the art review of the technologies associated with the development of EMI. Chapter 3 describes the hardware assembled in the experiments and LabVIEW program implemented to control the hardware. Then, the experimental set up and the measurements are presented in chapter 4. This chapter also presents the results of EMI analysis. Chapter 5 presents some conclusions and discussion about possible future research.

2.0 BACKGROUND OF EMI METHOD

2.1 PRINCIPLE OF EMI METHOD

A simplified 1-D model of the EMI method is illustrated in Fig. 2.1. In this figure, a PZT transducer is bonded to the surface of a host structure. When a voltage is applied to the PZT, the PZT generates a local stress parallel to the surface of the host structure, thus transmitting elastic waves to the structure. The structure response can be expressed by the drive-point mechanical impedance, which is the complex ratio between the applied force and velocity at the excitation point. Through the mechanical coupling between the PZT and the host structure and the electromechanical transduction of the PZT, the mechanical impedance of the host structure reflects to the electrical impedance which can be measured at the terminals of the PZT (Giurgiutiu et al., 1999). This approach indicates the structural mechanical impedance by measuring the electrical impedance of the PZT, thus named electromechanical impedance method.

The electrical admittance of the PZT ($Y(\omega)$), which is the inverse of the electrical impedance, can be expressed in the frequency domain as (Maruo et al., 2015):

$$Y(\omega) = i\omega a[\bar{\varepsilon}_{33}^{T} - \frac{Z_s(\omega)}{Z_s(\omega) + Z_a(\omega)} d_{3x}^2 \hat{Y}_{xx}^{E}] \tag{2.1}$$

In Eq. 2.1, the mechanical impedance (Z_a) represents the mechanical characteristic of the PZT patch. The driving point mechanical impedance (Z_s) refers to the mechanical

impedance of the host structure. ω is the excitation frequency; a is a geometry constant of PZT; d_{3x} is the piezoelectric strain constant of the PZT. $\bar{\varepsilon}_{33}^{T}$ is the PZT dielectric constant. $\hat{Y}_{xx}^{E}$ is the complex Young's modulus of the PZT with zero electric field (Maruo et al., 2015).

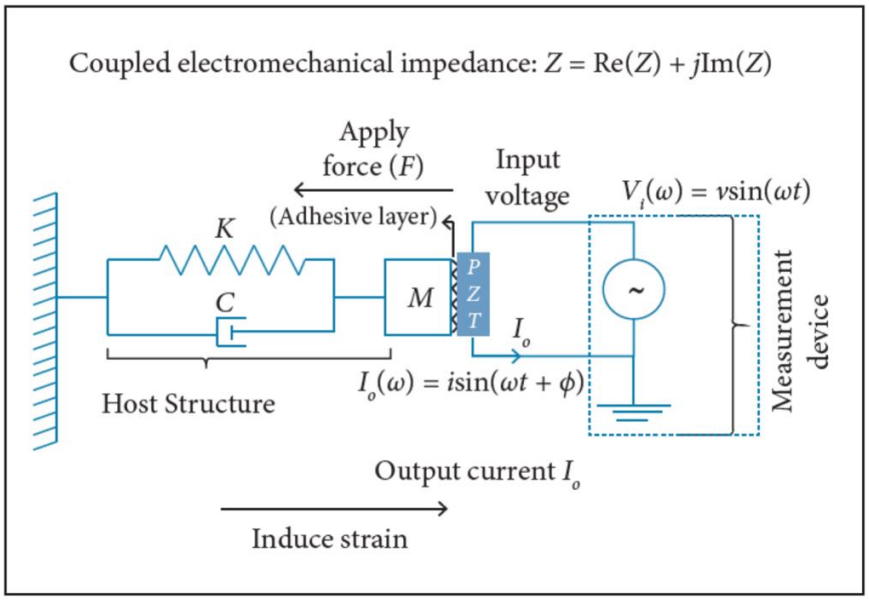

Figure 2.1 Schematic diagram of the electromechanical interaction between a PZT and the host structure to which the PZT bonded (Maruo et al., 2015)

When damage occurs in the host structure, the mass (M), stiffness (K) or damping (C) of the host structure change and this affects the mechanical impedance of the structure (Z_s). In Eq. 2.1, all other PZT characteristics do not change, only the variation of Z_s will change the electrical admittance value of the PZT patch. Thus, any variation in the measured admittance signature ($Y(\omega)$) of the PZT patch may indicate the presence of damage in the host structure. In this way, the electrical impedance variation of PZT patch provides an indication that the mechanical impedance of the structure has changed.

A schematic configuration of the PZT is shown in Fig. 2.2. In the 1-D model of Fig. 2.1, the harmonic voltage is applied along the 3-direction, and thus the relative mechanical strains and stresses are applied along the 1-2 plane. Thus, the relative electromechanical couplings are in the 3-1 and 3-2 planes.

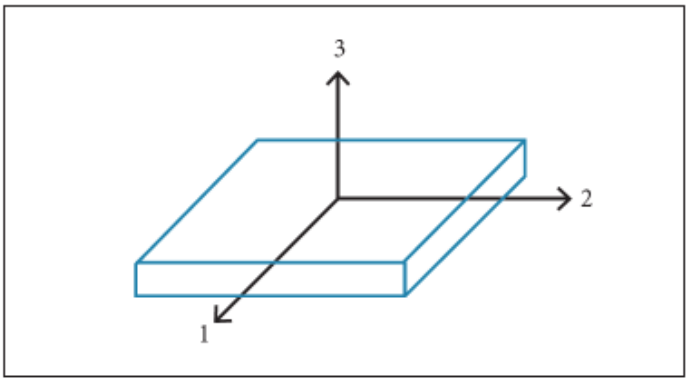

Figure 2.2 PZT transducer axis (Maruo et al., 2015)

2.2 DEVELOPMENT OF EMI METHOD

Liang et al. (1994) introduced the EMI method for SHM applications. The piezoelectricity of a ceramic material was employed to calculate the energy flow in an electromechanical spring-mass-damper system driven by a PZT actuator.

After this, researchers started to apply the EMI method for the detection of damage in many engineering systems. Giurgiutiu et al. (1999) observed the propagation of cracks in a specimen with one spot-welded joint. Twelve PZTs were attached to the specimen around the joint and the cracks were induced with a fatigue loading test. By control the fatigue cycling, the corresponding degree of cracks damage was applied to the structure.

The cracks progression, related to the loss of the structure stiffness, was observed through variation of the impedance signature. A series of data sets of the impedance signature was obtained including pristine and fatigued states. The results showed that the increase of cracks length leads to the increase of damage metric values.

Park et al. (2000) used the EMI technique to monitor composite-reinforced concrete wall. Five PZTs were attached on the surface of the wall and the results associated with the impedance signature demonstrated that the method could detect local damage. Park (2001) monitored a pipeline with several bolted junctions. A signal above 30 kHz was emitted through PZTs attached around the joints. Damage was simulated in terms of loose bolts that decreased the mechanical impedance of the system. The electrical impedance signatures relative to 2, 4, 6 and 8 loosen were measured and some statistical metrics were calculated to quantify any variation. The results showed that the metrics increased with the increase of the number of loose bolts.

Zagrai and Giurgiutiu (2001) applied the EMI method in a thin circular aluminum plate. Five different states of the plate were investigated including the pristine condition and four damage states with different crack locations. A PZT was bonded at the center of each plate and four crack locations were 3, 10, 25 and 40 mm away from the PZT respectively. The PZT impedance was measured using a HP 4194A Impedance Analyzer. The results showed that damage metric value increase as crack distance from the PZT decreases.

In the previous experiments, the PZT patch was considered perfectly bonded to the surface of the host structure. And the adhesive layer between the PZT and the structure was not considered. Thus, the force does not directly transfer from one medium to the other;

instead it transfers through the adhesive, which can cause shear lag. Bhalla and Soh (2004) took shear lag into consideration and developed a modified model of the PZT impedance. Different parameters related to the adhesive layer were investigated and the results demonstrated that the impedance signature changes significantly if the PZT patch is not attached properly to the host structure.

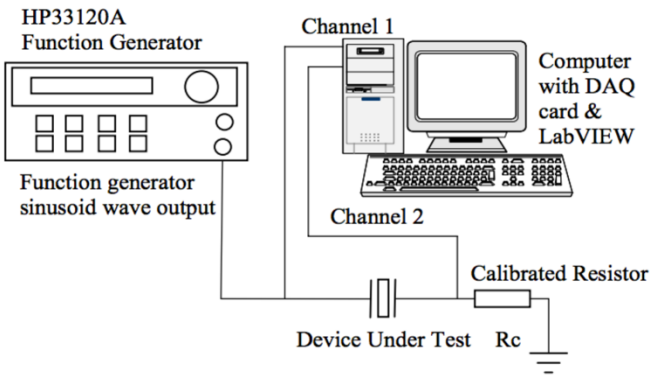

Figure 2.3 Impedance measurement system (Xu & Giurgiutiu, 2005)

An impedance analyzer, like the HP 4194A, is typically used for EMI monitoring. However, this conventional equipment is expensive and bulky. Some researchers proposed and developed alternative and more convenient measurement systems to replace the conventional impedance analyzer. Xu and Giurgiutiu (2005) created a SHM system shown in Fig. 2.3, to detect the disband of stiffeners in an aluminum panel, by employing a Data Acquisition (DAQ) and a Function Generator. A chirp signal and swept-frequency signal were generated as the actuation source to guarantee the accuracy of electromechanical impedance analysis. The impedance signature was calculated using transfer function and Fast Fourier Transform. The performance of this system is better when using swept-frequency signal as excitation, because the results matched the results obtained from HP

4194 better. Although the impedance signatures show a slight variation between these two measurements, the simulated damage, disbond, can be detected by the proposed system.

Park at el. (2007) proposed some advanced signal-processing to inspect the loose bolts in an aluminum structure using wireless PZTs in a SHM system. They employed principal component analysis (PCA) algorithm in data compression and clustering-based pattern k-means recognition in the post signal processing part. This improvement in the signal processing process can eliminate the unexpected electromechanical or environmental noise. Through using the PCA-data compression and K-means recognition algorithms, the RMSD-based detection showed more capability than the results obtained from the raw data without any post processing. Another advancement of this study is that an impedance board (AD5933) was used, which is low-cost (nowadays about $100) and convenient for in-situ inspection.

Bhalla and Gupta (2009) proposed a novel and economical hardware to measure the electromechanical impedance. The hardware was composed of a function generator, a digitizer and a circuit. In this study, only the real part of admittance was detected by using a Fourier transform (FFT) analyzer. Two types of measurements were conducted, one was employing the presented hardware and the other was using LCR meter for measurements. The accuracy of the results using the presented hardware was guaranteed after comparing with the impedance signature obtained by LCR meter. Panigrahi et al. (2010) employed a SHM system including a function generator, a mixed signal oscilloscope and a circuit to detect the drilling holes in an aluminum section. The results showed that this system could detect damage occurrence and development in the aluminum section0.

Baptista et al. (2011) noticed that the effect of PZT size was not investigated in EMI testing method. A theoretical analysis of the optimal PZT size was carried out. In addition, to validate the theoretical results, a series of experiments regarding different PZT sizes was conducted. The theoretical and experimental results matched well and showed that the PZT size, for structures with low damping, must be small to guarantee the sensitivity of detection.

Since 2011, researchers started to integrate the EMI with other methods, such as GUWs method. GUWs method is sensitive to small damage in a relatively large detection field. An and Sohn (2011) presented an integrated SHM system based on both EMI and GUWS methods. Two simultaneous measurements were obtained from one single hardware, including a function generator, a digitizer and a circuit. In addition, the effect of the temperature on these two measurements were also addressed by compensating the passive part of the complex impedance results. And using the compensation algorithm, two damage conditions, loosening bolt and crack, were investigated in metallic structures in various temperature range from -20 to 70 °C.

An et al. (2012) monitored the experiments a composite airplane wing by employing both EMI and GUWs method to detect the structural hot spots, areas that are inaccessible with high stress concentration. To validate this IIG system, a real and full-size airplane wing was manufactured and detected in this study. During the manufacturing process of the wing, the hot spots, with high stress concentration, were located using finite element method. The PZT patches were permanently attached around the hot spots. Various damage situations, including composite skin spalling and blot loosening, were

investigated under different temperature. The service life of PZT was also considered by a self-diagnosis analysis in this study to guarantee the durability of the SHM system.

Zhu and Rizzo (2012) proposed a unified SHM system incorporating EMI and GUWs methods using a National Instrument (NI)-PXI running under LabView. This system was relatively convenient to operate because only one hardware (NI-PXI) was used. In addition, the input, output, pre-processing and storage of signal are all controlled by one single LabVIEW program. An aluminum plate and a steel pipe under various damage states with different boundary conditions were monitored. The experimental results demonstrated that the unified SHM system is reliable and should be applied to SHM system for real-time detection.

Gresil at el. (2012) presented a finite element model for the damage detection of composite materials. This model, based on multi-physics (MP-FEM), simulates the electromechanical signature of the PZT and the interaction between the PZT patch and the glass fiber reinforced polymer (GFRP) composite segment. The MP-FEM 3D model was validated to be feasible through comparing to experimental results using conventional impedance analyzer. In addition, the impedance signatures in other conditions like the deterioration of adhesive layer or PZT itself were also investigated. The results show that the impedance signatures are consistent both for low and high frequencies. However, the damping coefficient in the 3D MP-FEM model has different influence on the impedance signatures with low and high frequencies. Gresil and Giurgiutiu (2014) investigated this 3-D MP-FEM model and concluded that this model show high robustness at high frequency and damping plays an important role.

Gulizzi and Rizzo (2015) integrated EMI and GUWs methods. Using a National Instrument NI-PXI and controlled by LabView program in an aluminum plate. In this study, three damage sizes in different locations were simulated by adding aluminum mass using magnet. Three experimental results including pitch-catch signal, pulse-echo signal, and EMI impedance signature were obtained simultaneously. A weighted metric value was presented based on the three approaches to illustrate the damage severity and locations in the aluminum plate. The results showed that this set-up is robust and can be applied in the online SHM system.

Maruo et al. (2015) proposed the hardware schematized in Fig. 2.4 to measure the electromechanical impedance of multiplex transducers. In this set up, high-speed DAQ and Fast Fourier Transform analyzers are not needed, which reduce the cost for equipment. A low-cost integrated circuit and a digital signal processor were constructed and applied to an aluminum beam and an aircraft panel. The real part of the impedance was extracted from the ratio between the time variant portion of the instantaneous power waveform and the root mean square current. The performance of this prototype was compared to the results obtained with an impedance analyzer and proved to be reliable.

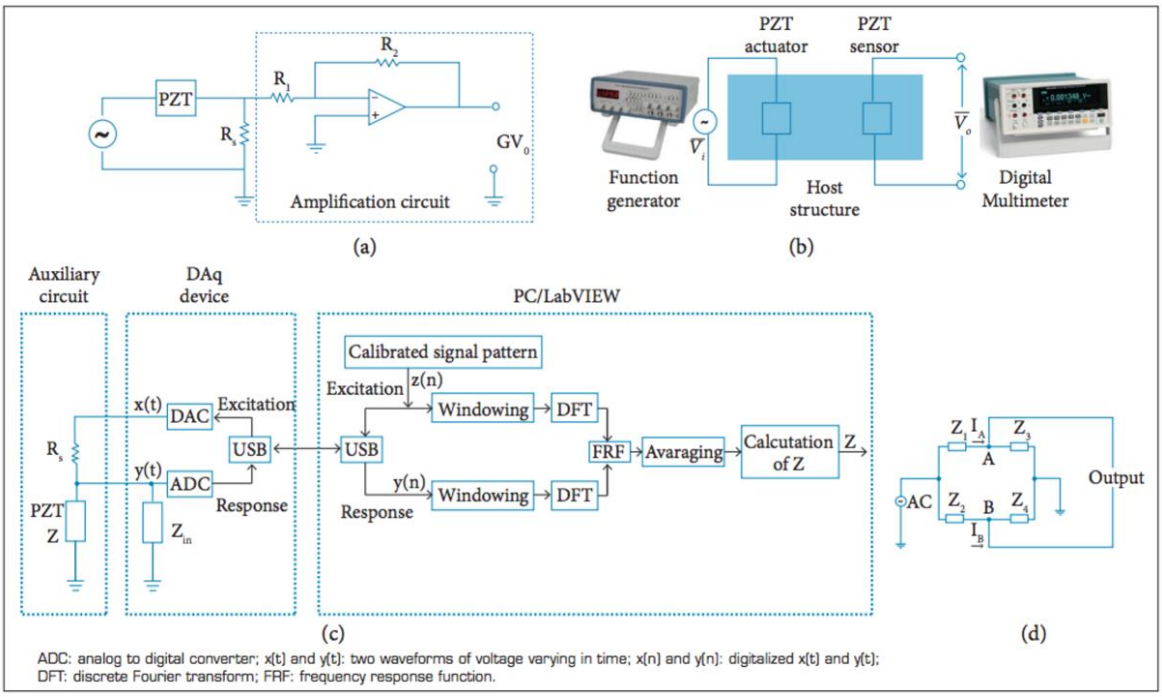

Figure 2.4 Impedance measurement system (Maruo et. al., 2015)

EMI technique can monitor a relative small area around the PZT. As such, the cost of the monitoring would be proportional to the volume of the host structure. To address this limitation, Na and Park (2016) proposed a low-cost EMI technique by using an analog device (AD 5933) to monitor multiple areas. The PZT patches were connected to the AD 5933 board directly and attached to an aluminum plate. The damage progression in the testing was simulated by cutting 1 mm to 10 mm at one edge of the plate. By setting up a threshold value for damage metric value, the simulated damages were all detected. The damage metric value increased as the progression of the cut.

Kettle (2016) used a finite element method (FEM) to first carry out fundamental simulations of simple structures like free PZTs with various shapes and thicknesses. Then, practical scenarios where different parts of the host structure subjected to damage and external load were simulated. Finally, the effect of temperature was investigated.

3.0 EXPERIMENTAL SETUP

In this chapter, the hardware design to drive the integrated SHM system is described in detail. As six transducers are employed in the experiment, the relevant schematic diagram is illustrated and the working principle of the SHM system is explained by choosing the situation that one of the six PZTs as actuator. The algorithm used to extract the impedance signature of PZTs is presented.

3.1 HARDWARE DESIGN

The hardware employed to integrate the EMI and GUWs methods is shown in Fig. 3.1 and consists of two parts: the actuating part and the receiving part. The integrated system is driven by a National Instruments PXIe 1062Q (NI PXI) shown in Fig. 3.2. A NI PXI-5412 Arbitrary Waveform Generator (AWG) is used to excite the PZTs. An 8-channel NI PXI-5105 digitizer is used to digitize the detected signals. The PXI also contains a NI PXIe-8108 controller.

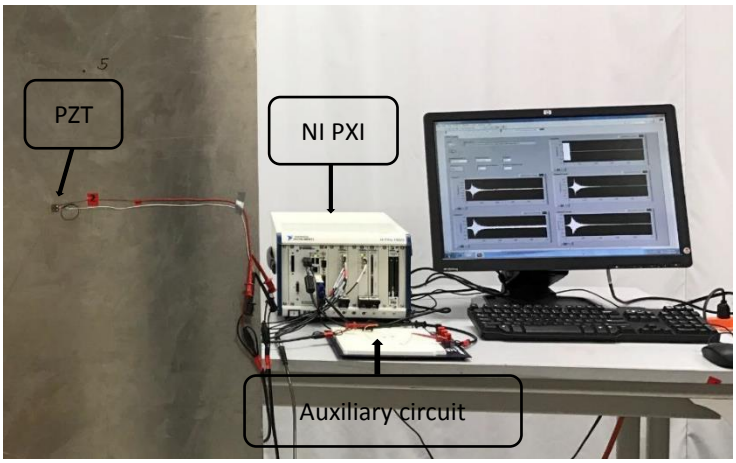

Figure 3.1 The integrated SHM system

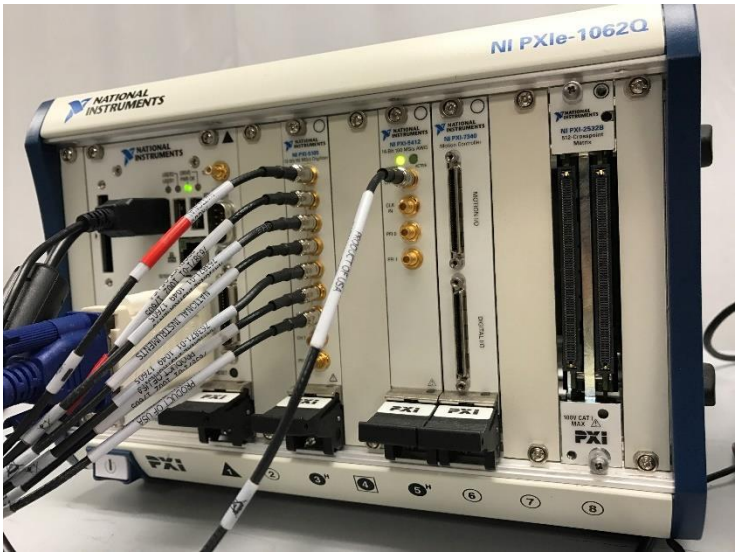

Figure 3.2 NI PXIe-1062Q

The actuation part consists of the AWG and an auxiliary circuit displayed in Fig 3.3. The auxiliary circuit contains a resistor as a voltage divider, which is shown in Fig. 3.4. A BNC T-connector splits the output of the AWG to the channel 0 of the digitizer and to the circuit. The latter is linked with the minigrabber connector A in Fig. 3.3. After

passing through the resistor R_s, the voltage signal is transmitted through the actuator using the minigrabber connector B (Fig. 3.3 and Fig. 3.5).

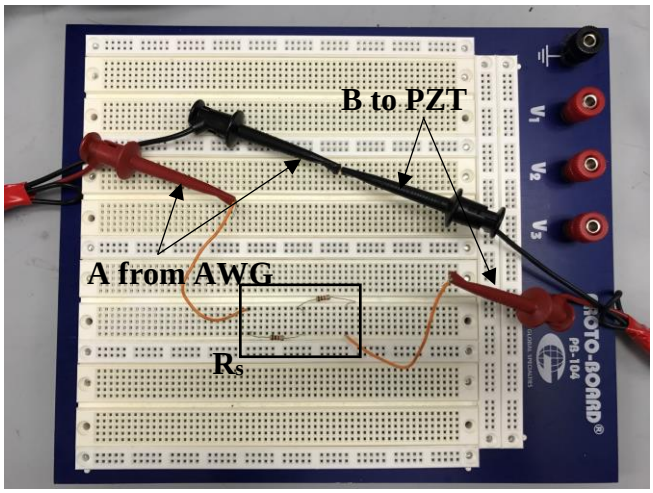

Figure 3.3 Resistor in the auxiliary circuit with minigrabber connector A connected to the AWG, and minigrabber connector B connected to the actuator PZT

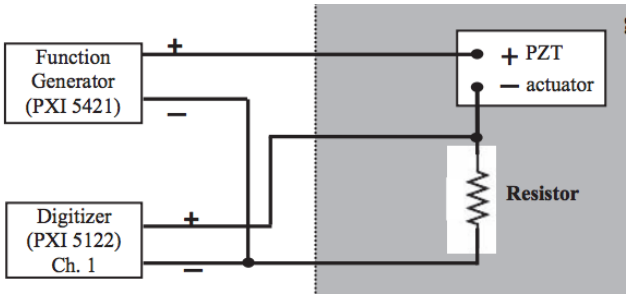

Figure 3.4 Voltage divider circuit (Zhu and Rizzo, 2012)

Figure. 3.5 shows that the terminals of the PZT are connected to the circuit with the minigrabber connector B and to one channel of the digitizer with minigrabber connector C. The red wire refers to positive pole and the white wire refers to negative pole of the PZT. The arrangement enables each transducer of the array to act as actuator and receiver at the same time.

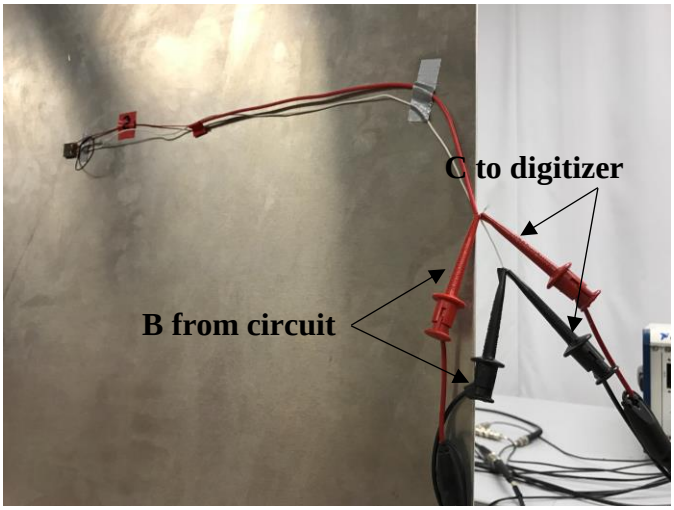

Figure 3.5 Actuator PZT with minigrabber connector B connected to the circuit (connected to the AWG), and minigrabber connector C connected to the digitizer

3.2 SCHEMATIC DESIGN FOR THE PRESENTED SHM SYSTEM

In the SHM system presented in this thesis, we used six PZTs. To describe the working principle of this system, Figure 3.6 presents the schematic diagram when PZT 2 served as the actuator. In the figure, $x(t)$ represents the analog signals, R_s is the resistor of the auxiliary circuit and equal to 1967 Ω, r_1 and r_2 represent the electrical resistances of cables, Z_{in} is the impedance of the PXI's digitizer, which consists of a resistance R_p in parallel with a capacitance C_p. According to the manufacturer, R_p=1×10^6 Ω and C_p=1×10^{-10} F.

Figure 3.6 schematizes the situation which PZT 2 is connected to the auxiliary circuit and works as actuator (PZT_a). For each measurement, the AWG delivered a chirp that is stored by channel 0 of the digitizer as $x_0(t)$. After passing through the auxiliary circuit, $x_0(t)$ splitted into the instantaneous voltage $x_a(t)$ sent to PZT_a and sent to channel 2 of the

digitizer. The signal transmitted by PZT_a is detected as lamb waves $x_{sj}(t)$ by the remaining five PZTs and digitized as $x_i(t)$ (i=1…, NT; NT: number of the transducers) by the digitizer.

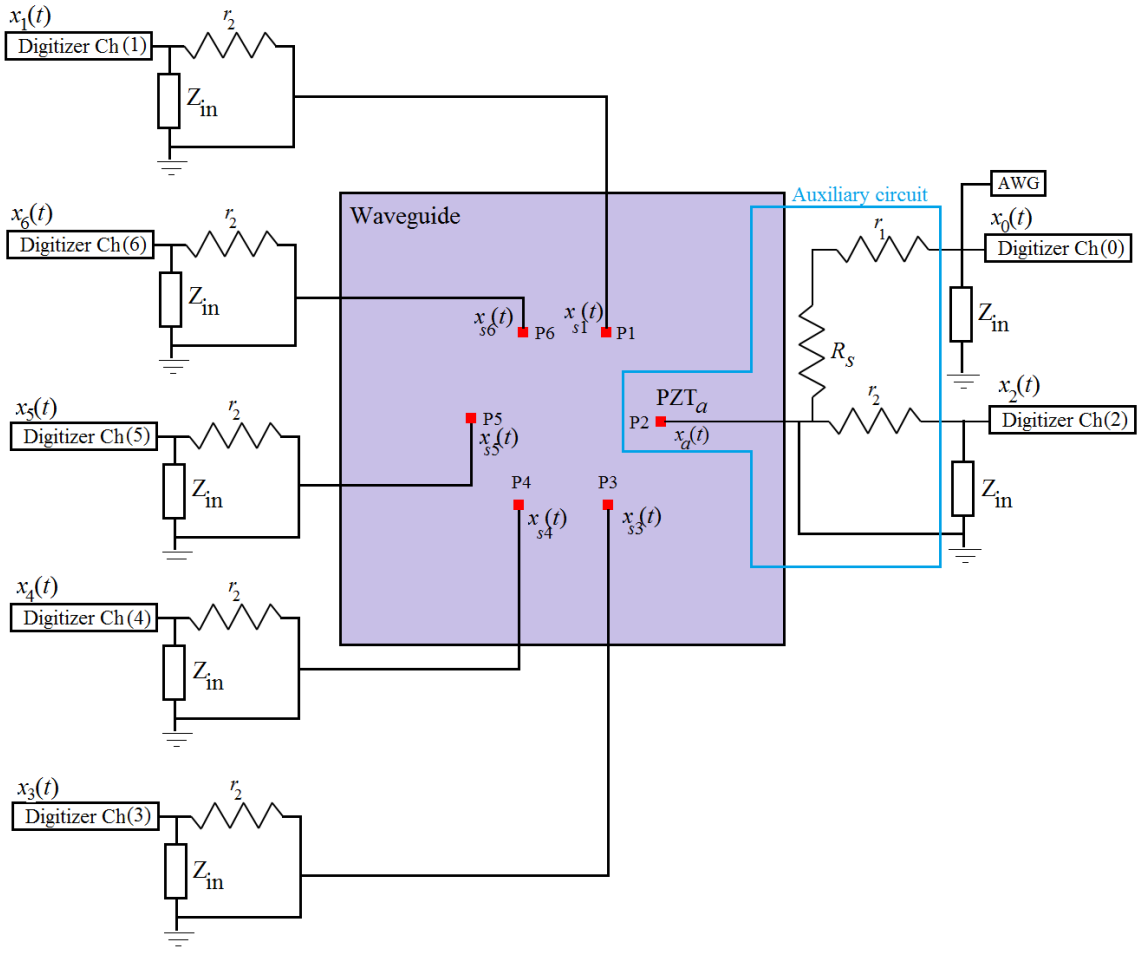

Figure 3.6 The schematic diagram of the integrated SHM system with six transducers

The received guided wave signals $x_i(t)$ of the six PZTs can be used for image processing of GUWs analysis, while the actuation signals $x_a(t)$ can be used for EMI analysis. In this way, the information for both GUWs and EMI analysis can be obtained simultaneously by run one experiment

3.3 EXPERIMENTAL MARERIALS

The tested aluminum plate is 1219mm×1219mm×2.54mm. Six 10mm×10mm×2mm PSI 5A4E transducers are bonded to form a hexagon around the center of the plate as shown in Fig. 3.7. The damage is simulated by gluing two 25.4 mm×25.4 mm×1.27 mm aluminum strips mass to the plate as shown in Fig. 3.8. Six PZTs are glued intimately to the surface of the testing aluminum plate. Between the PZT and the plate, a small piece of copper foil is attached to connect the negative electrode of the PZT to a wire, which is used as the PZT terminal. To evaluate the reliability of the integrated system, six damage locations are chosen to carry out the experiments, which are shown in Table 3.1.

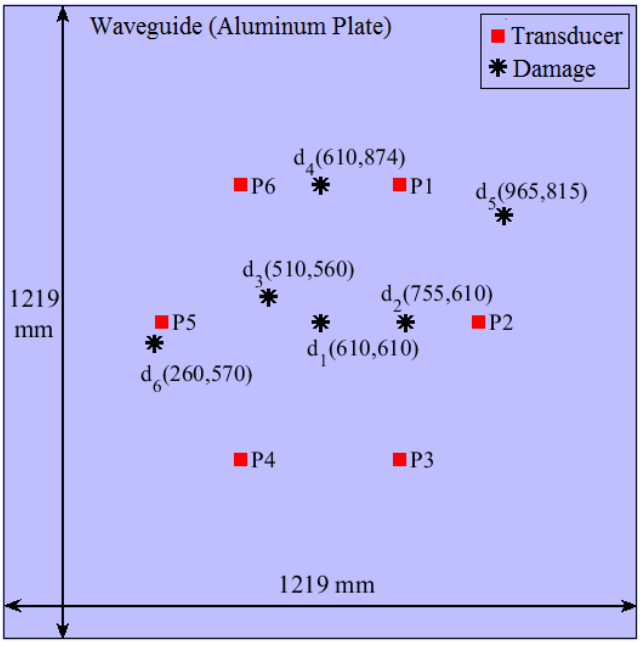

Figure 3.7 The schematic diagram of 6 PZTs arrangement and 6 damage locations

Table 3.1 The location of the damages with respect to the bottom left corner of the plate

Damage Number	x (mm)	y (mm)
1	610	610
2	755	610
3	510	560
4	610	874
5	965	815
6	290	570

A 24 V_{pp} amplitude chirp signal covering the frequency range from 90 kHz to 200 kHz of 1200 cycles is chosen as the excitation. The length of the chirp is 8 ms, total signal duration is equal to 100 ms. The sampling frequency is set as 2 MHz to get a high resolution of the experiment result.

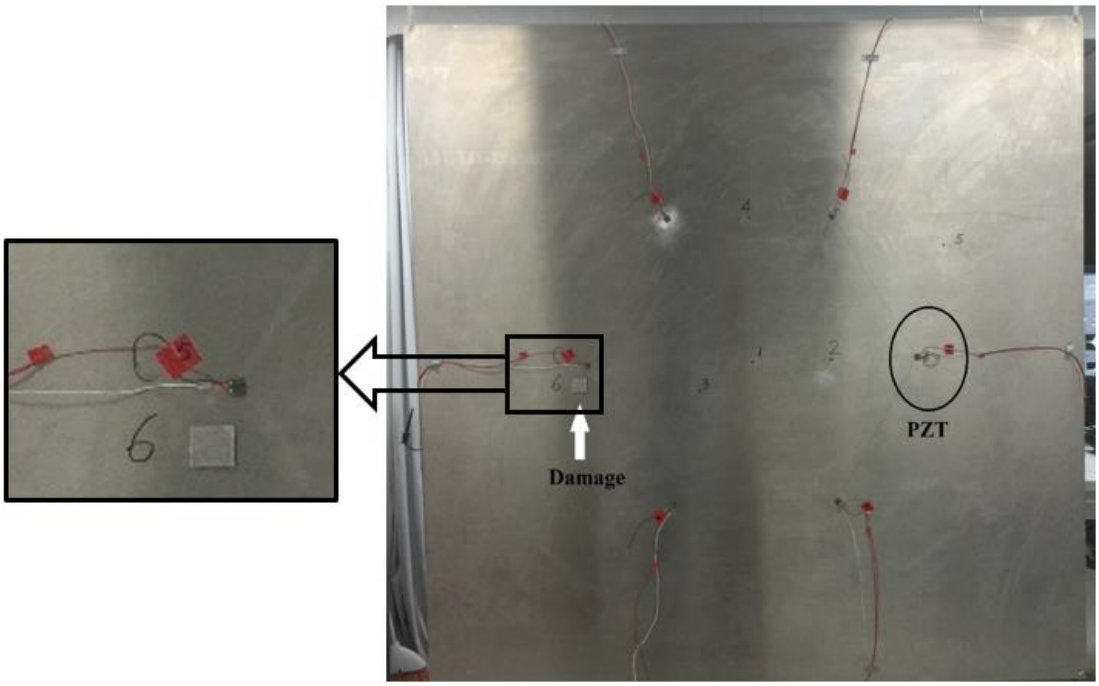

Figure 3.8 The test aluminum plate with the PZTs and damage 6

3.4 LABVIEW IMPLEMENTATION

3.4.1 Chirp Signal Generation

As is said earlier, a chirp signal is employed to excite the PZTs. Benefited from the broadband properties of chirp signal, the guided wave response of the receivers and the electromechanical response of the actuator can be obtained from one single experiment.

The chirp signal $x_0[n]$ is defined as (Gulizzi et al. 2015):

$$x_0[n] = Aw[n] \sin\left[\frac{2\pi}{f_s} n \left(\frac{f_2 - f_1}{2N} n + f_1\right)\right], \quad n = 0, \ldots, N-1 \tag{3.1}$$

Here, $w[n]$ represents a window function, f_s is the sampling frequency, A is the amplitude, and f_1 and f_2 are the start and the end frequency of this chirp signal. The total time of the chirp signal can be calculated as N/f_s. N is related to the number of cycles (N_c) of the signal itself and can be expressed as: $N = 2N_c f_s/(f_1 + f_2)$.

In this study, $f_s = 2$ MHz; $f_1 = 90$ kHz; $f_2 = 210$ kHz; $A = 24\ V_{pp}$; $N_c = 1200$; $N/f_s = 8$ ms; The duration of this chirp signal is 100 ms.

Eq. (3.1) is built in the LabVIEW diagram shown in Fig. 3.9 and the front panel shown in Fig. 3.10. The main step to generate the chirp signal is the loop to form a digital signal with 200,000 data samples. The sampling frequency is kept consistent by connecting the sampling frequency wire in the chirp signal with those in the niFgen and niScope part that are used to control the generation and detection of guided waves. The sampling frequency wire is identified with a blue arrow in Fig. 3.9.

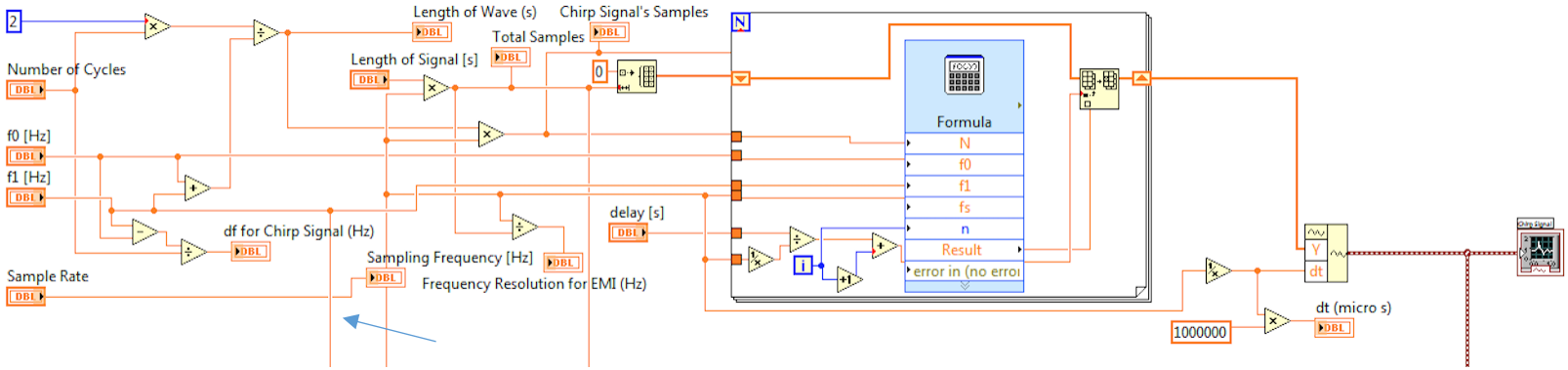

Figure 3.9 The generation of digital chirp signal in the diagram of LabView

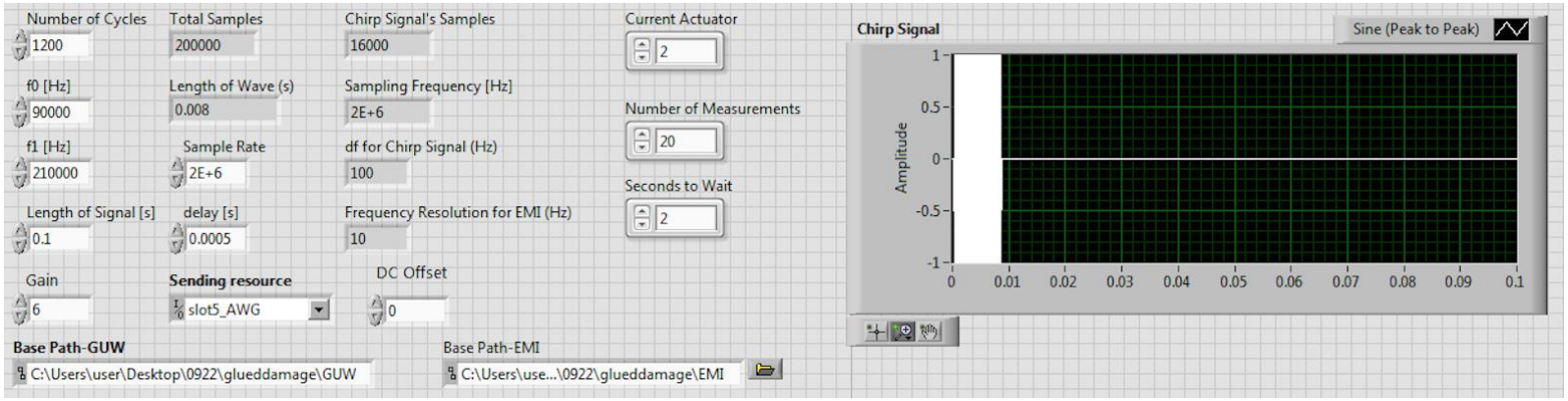

Figure 3.10 Front panel of the selection of the chirp signal parameters

3.4.2 GUWs Measurement

A function generator (FGEN) is inserted in the diagram to control the AWG to generate the chirp signal. LabVIEW has a FGEN express to control the AWG. This express function needs to be opened every time the users need to change the parameters of the FGEN. To make the program more interactive we create our own front panel. Our program uses a series of niFgen configurations.

First, an initial niFgen configuration is used to initialize the FGEN by choosing the input as the relative AWG resource. Then, the niFigen Configure Output Mode vi is used to set the output mode as arbitrary waveform. The niFgen Clear Arbitrary Memory vi is employed to remove all previously created arbitrary waveforms. Then, the critical configuration is niFgen Create Waveform. Here, the chirp signal (the red line) goes into the FGEN through the niFgen Create Waveform. After this step, the command for AWG to generate chirp signal has been transmitted to the hardware AWG. The block diagram of these steps is shown in Fig. 3.11.

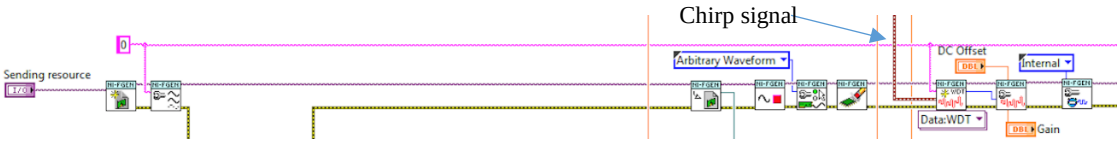

Figure 3.11 The niFgen configuration

At the same time, the digitizer records the signals detected simultaneously by the PZTs. The digitizer is also controlled by a configured oscilloscope established in the LabVIEW program. The configuration steps are similar to FGEN configuration.

Considering the vertical ranges of received signals are significantly different due to the big variation between the EMI response for the actuator and the GUWs response for the receivers, the customized niScope configuration block shown in Fig. 3.12 is used to address this problem. In addition, since each PZT serves as actuator once and provides corresponding EMI response, a Case structure is implemented in the block diagram to determine the current actuator and assign the appropriate vertical range to different transducers. Another critical step is the niScope Multi Fetch WDT vi, as shown in Fig. 3.12, which enables the hardware digitizer to read and record the received signals from different transducers.

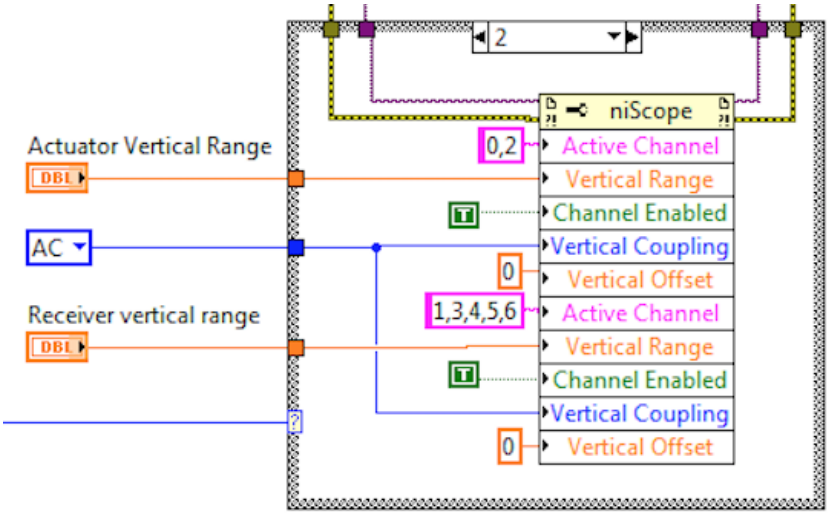

Figure 3.12 Case structure for each niScope configuration relative to current PZT actuator

Another important issue is to synchronize the input and output. This is done by adding the niTClk in the block diagram as shown in Fig. 3.13. The niTClk Configure For Homogeneous Triggers vi is used to guarantee the input and output signals share the same trigger. The niTClk Synchronize vi is employed to synchronize the TClk signals on the given sessions: the input and output signals in this program.

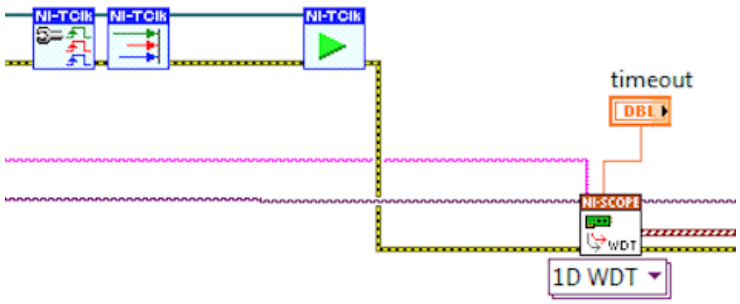

Figure 3.13 The niTClk Configuration and the niScope Multi Fetch WDT vi

To minimize the influence of noise, 20 measurements are carried out using a For loop in the program. Thus, the signal recorded by the digitizer for each channel is the mean value of the 20 measurements. The signals received by the digitizer for all channels need to be separated and saved for each PZT after one experiment. After this, the end command by using FGEN Abort for AWG and oscilloscope Abort configuration for digitizer will be send to the PXI and the program will be stopped.

To observe the received response, the graphs of all the input and output waveforms are shown in the front panel of Fig. 3.14. The figure displays the case when the PZT 2 is the actuator and all the PZTs including PZT 2 act as receivers. The top right chart shows the generated chirp. Graph channel 1 refers to the one-time measurement of the PZT 1 response, while the channel 1 (mean) refers to the mean-value of n (n=1, 2…,20) measurements in real time. Graph channel 2 shows the EMI response of the current actuator PZT 2.

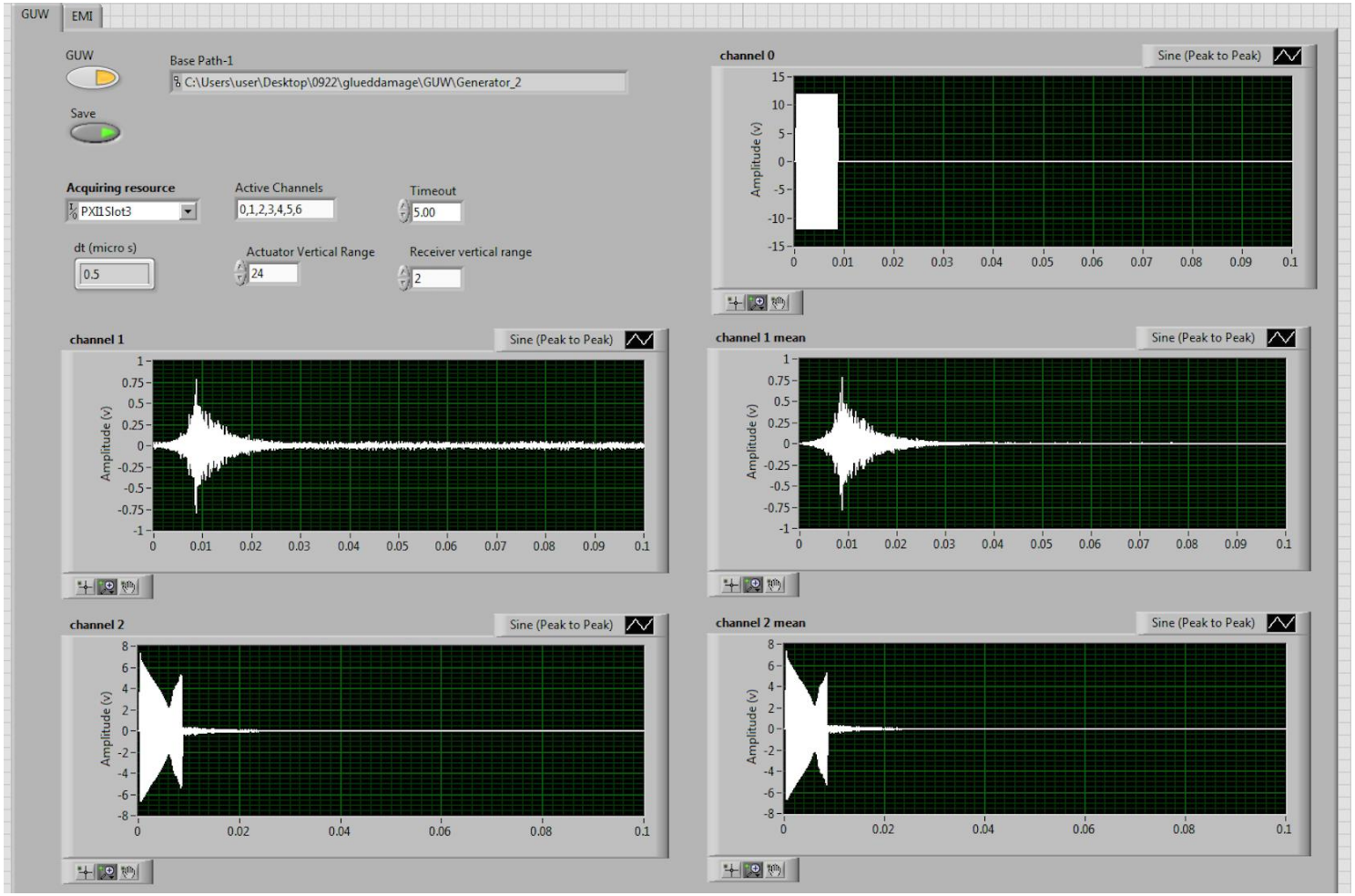

Figure 3.14 Response of GUWs when PZT 2 as the actuator

3.4.3 EMI Measurements

All the codes applied in the GUWs part are shared with by the EMI part of the integrated system. The same setup: excitation chirp signal, niFgen and niScope configuration, times of measurements, are used in the EMI part simultaneously during the experiment. For EMI measurement, however the calculation of the frequency response function (FRF) $\mathrm{H}_{i0}[\mathrm{K}]$ is needed when calculating the impedance signature of the actuator PZT. $\mathrm{H}_{i0}[\mathrm{K}]$ can be calculated as the ratio between the discrete Fourier transform (DFT) of each signal to the DFT input signal (Gulizzi et al. 2015).

$$\mathrm{H}_{i0}[\mathrm{K}] = \frac{\mathrm{X}_i[\mathrm{K}]}{\mathrm{X}_0[\mathrm{K}]}, \qquad i = 1, \dots, NT; \tag{3.2}$$

here, $\mathrm{X}_i[\mathrm{K}]$ refers to the DFT of the EMI response of the ith PZT transducer*:* $x_i(t)$ (i=1,…,NT; NT: number of PZT); $\mathrm{X}_0[\mathrm{K}]$ refers to the DOF of the input signal: $x_0(t)$.

The built-in Frequency Response Function (Mag and Phase) vi is used to calculate the FRF $\mathrm{H}_{i0}[\mathrm{K}]$. For each PZT actuator, during the GUWs measurement, the EMI response $x_i(t)$ is also recorded by the ith channel of the digitizer and the input signal $x_0(t)$ is recorded by channel 0 of the digitizer. The data are saved before the next round of measurement: the next actuator emits input to the system. A parameter is used to lock the current actuator by setting the input as the current actuator number. This parameter appears as Current Actuator in the front panel as shown in Fig. 3.10; thus, users can choose any PZT as actuator by simply change the parameter from 1 to 6. A case structure is used as a switch to enable the EMI measurements as shown in Fig. 3.15.

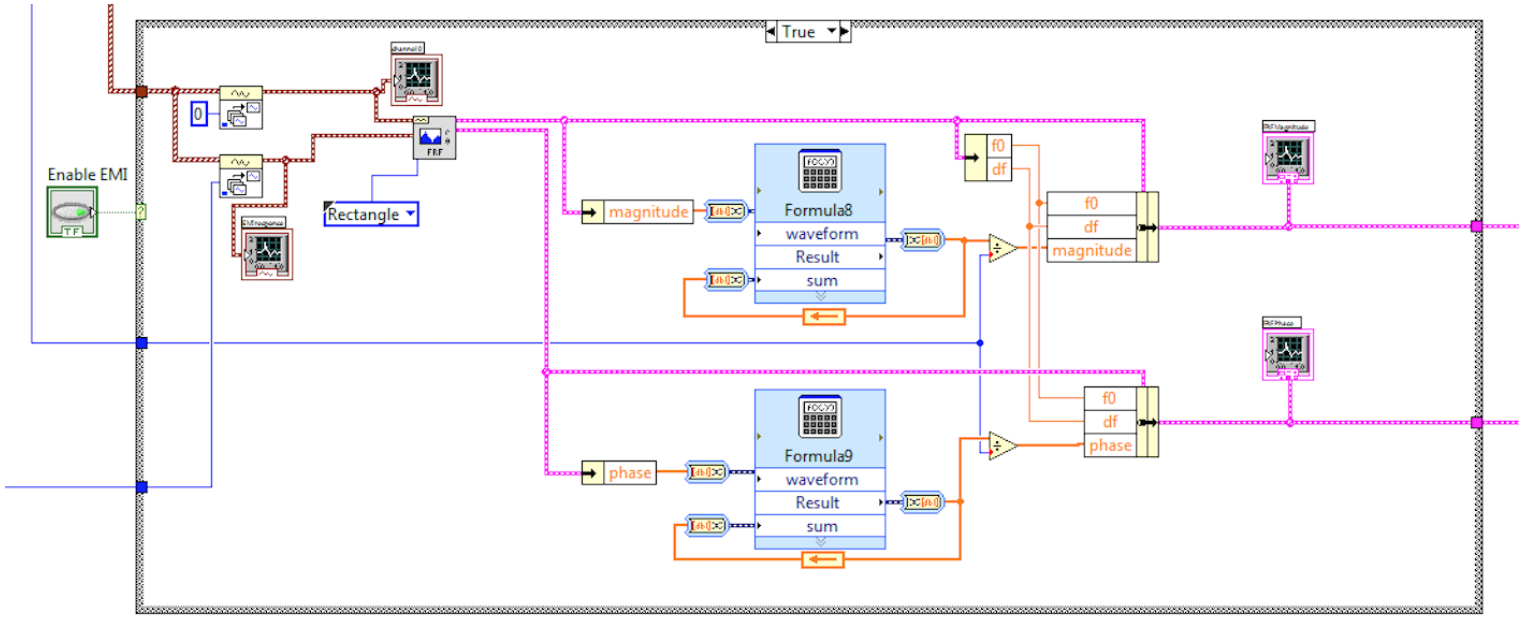

Figure 3.15 Case structure for EMI FRF calculation

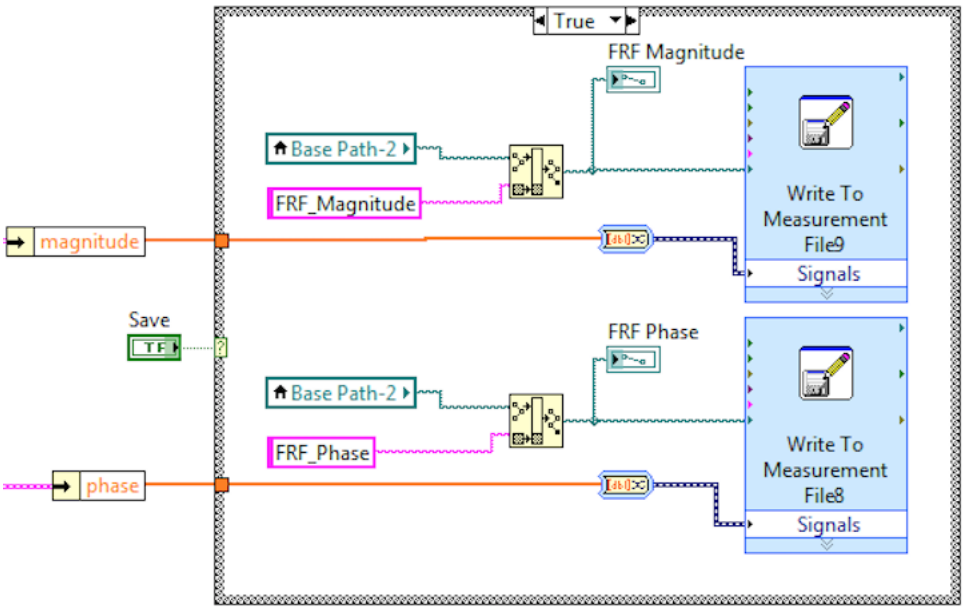

Figure 3.16 Data save for the FRF

As shown in Fig. 3.10, the current actuator is PZT 2. Thus, two corresponding inputs $x_2(t)$ and $x_0(t)$ come into the FRF tool shown in Fig. 3.15. Then, the outputs including magnitude and phase angle of this FRF $H_{20}[K]$ will be obtained and saved to relative files shown in Fig. 3.16.

By employing this LabVIEW program, the automatic measurements for both GUWs and EMI response can be obtained through one single run of the experiment. The real-time information of these two methods can be obtained simultaneously by employing one experiment setup, including one chirp signal, the same AWG and digitizer, is employed in the program. GUWs and EMI measurements can also be implemented separately using this program by two switches shown in the front panel, which is very convenient for the users.

3.5 ALGORITHM DESIGN

3.5.1 Impedance Signature Extraction of PZT

The FRF $H_{i0}[k]$ can be expressed by the electrical impedance of the actuator PZT. The derivation based on the schematic diagram in Fig. 3.5 is shown below.

$$H_{i0}[k] = \frac{X_i[k]}{X_0[k]}, \qquad i = 0, 1, \dots NT \tag{3.3}$$

$$H_{i0}[k] = \frac{X_i[k]}{X_0[k]} = \frac{V_i[k]}{V_0[k]} = \frac{i[k](Z_a[k])}{i[k](Z_t[k])} \tag{3.4}$$

Here, $Z_a[k]$ is the impedance of the auxiliary circuit, $Z_t[k]$ is the total impedance of the experiment circuit.

$$Z_a[k] = \frac{Z_{i,PZT}[K](r_2 + Z_{in}[k])}{Z_{i,PZT}[K] + r_2 + Z_{in}[k]} \tag{3.5}$$

$$Z_t[k] = Z_a[k] + R_s + r_1 = \frac{Z_{i,PZT}[K](r_2 + Z_{in}[k])}{Z_{i,PZT}[K] + r_2 + Z_{in}[k]} + R_s + r_1 \tag{3.6}$$

Here, $Z_{i,PZT}[K]$ is the impedance of the i^{th} actuator PZT, r_1 and r_2 are the resistance of the connection wires, $Z_{in}[k]$ is the impedance of the digitizer and R_s is the resistor employed in the auxiliary circuit.

Substitute Eq. (3.5) and (3.6) into (3.4), gives,

$$H_{i0}[k] = \frac{i[k]\dfrac{Z_{i,PZT}[K](r_2 + Z_{in}[k])}{Z_{i,PZT}[K] + r_2 + Z_{in}[k]}}{i[k]\left(\dfrac{Z_{i,PZT}[K](r_2 + Z_{in}[k])}{Z_{i,PZT}[K] + r_2 + Z_{in}[k]} + R_s + r_1\right)} \tag{3.7}$$

Which is,

$$H_{i0}[k] = \frac{Z_{i,PZT}[K](r_2 + Z_{in}[k])}{Z_{i,PZT}[K](R_s + r_1 + r_2 + Z_{in}[k]) + (R_s + r_1)(r_2 + Z_{in}[k])} \tag{3.8}$$

Here, r_1 and r_2 are the resistance of the wires which are trivial in this experiment, thus, let $r_1 = r_2 = 0$ in this set up. The Eq. (3.8) can be written as,

$$H_{i0}[k] = \frac{Z_{i,PZT}[K]Z_{in}[k]}{Z_{i,PZT}[K](R_s + Z_{in}[k]) + R_s Z_{in}[k]} \tag{3.9}$$

Thus, $Z_{i,PZT}[K]$ can be solved from Eq. (3.9), which is,

$$Z_{i,PZT}[k] = \frac{H_{i0}[k]Z_{in}[k]R_s}{Z_{in}[k] - H_{i0}[k](R_s + Z_{in}[k])} \tag{3.10}$$

The $H_{i0}[k]$ in Eq. (3.10) can be obtained from the EMI measurement in the LabView program based on Eq. (3.2). Thus, the impedance signature of each PZT can be extracted from this integrated system.

In the data analysis presented in this thesis, the conductance $G_{i,PZT}[k]$, which is the real part of admittance, is used for the calculation of the damage metric. The admittance is calculated as:

$$Y_{i,PZT}[k] = \frac{1}{Z_{i,PZT}[k]} \tag{3.11}$$

And the conductance $G_{i,PZT}[k]$ is

$$G_{i,PZT}[k] = Re(Y_{i,PZT}[k]) \tag{3.12}$$

3.5.2 Evaluation of Impedance Variation Using Damage Metrics

Two stages of the aluminum plate are considered: pristine and damage states. The damage state refers to the situation in which two aluminum strips are glued to both sides of the plate at various locations.

Four different damage metrics are computed to perform the damage detection,

1. The root mean square deviation (RMSD) (Park, et al. 2003):

$$RMSD = \sqrt{\frac{\sum_{k=1}^{n}\left(G_p[k] - G_d[k]\right)^2}{\sum_{k=1}^{n}\left(G_p[k]\right)^2}} \times (100\%) \tag{3.13a}$$

2. The average square difference (ASD) (Raju, 1997):

$$ASD = \sum_{i=1}^{n}\left(G_p[k] - \left(G_d[k] - \left(\bar{G}_p[k] - \bar{G}_d[k]\right)\right)\right)^2 \tag{3.13b}$$

3. The mean absolute percentage deviation (MAPD) (Tseng and Naidu, 2002):

$$MAPD = \sum_{k=1}^{n}\left|\frac{G_p[k] - G_d[k]}{G_p[k]}\right| \tag{3.13c}$$

4. The sum of the average difference (M) (Peairs, 2002):

$$M = \sum_{k=1}^{n}\left(G_p[k] - G_d[k]\right)^2 \tag{3.13d}$$

In Eq. (3.13), $G_p[k]$ and $G_d[k]$ are the real part of the admittance, the conductance, of the actuator in the pristine and the damaged states, respectively. $\bar{G}_p[k]$and $\bar{G}_d[k]$ are the mean value of the conductance of the actuator in the pristine and the damaged states, respectively. k is the total number of points in the considered frequency range.

4.0 EXPERIMENTAL RESULTS

First, the properties of the six PZTs are evaluated. Then, the results relative to the test of the aluminum plate with and without damage are presented.

4.1 EVALUATION OF THE SIX TRANSDUCERS

Before the experiment, the similarity of the employed transducers is evaluated using the algorithm in sections 3.5.1 and 3.5.2. The conductance and suspectance of the six transducers under free boundary conditions are measured and are presented in Fig. 4.1 (a) and (c).

After the transducers are bonded to the pristine plate, the impedance signatures are measured to evaluate the repeatability of the setup. The results are shown in Fig. 4.1 (b) and (d). The impedance signatures of the six free PZTs show that the transducers are approximately identical in terms of amplitude and resonant frequency. As expected, the amplitudes at the resonant frequencies are significantly smaller after the PZTs are bonded to the plate.

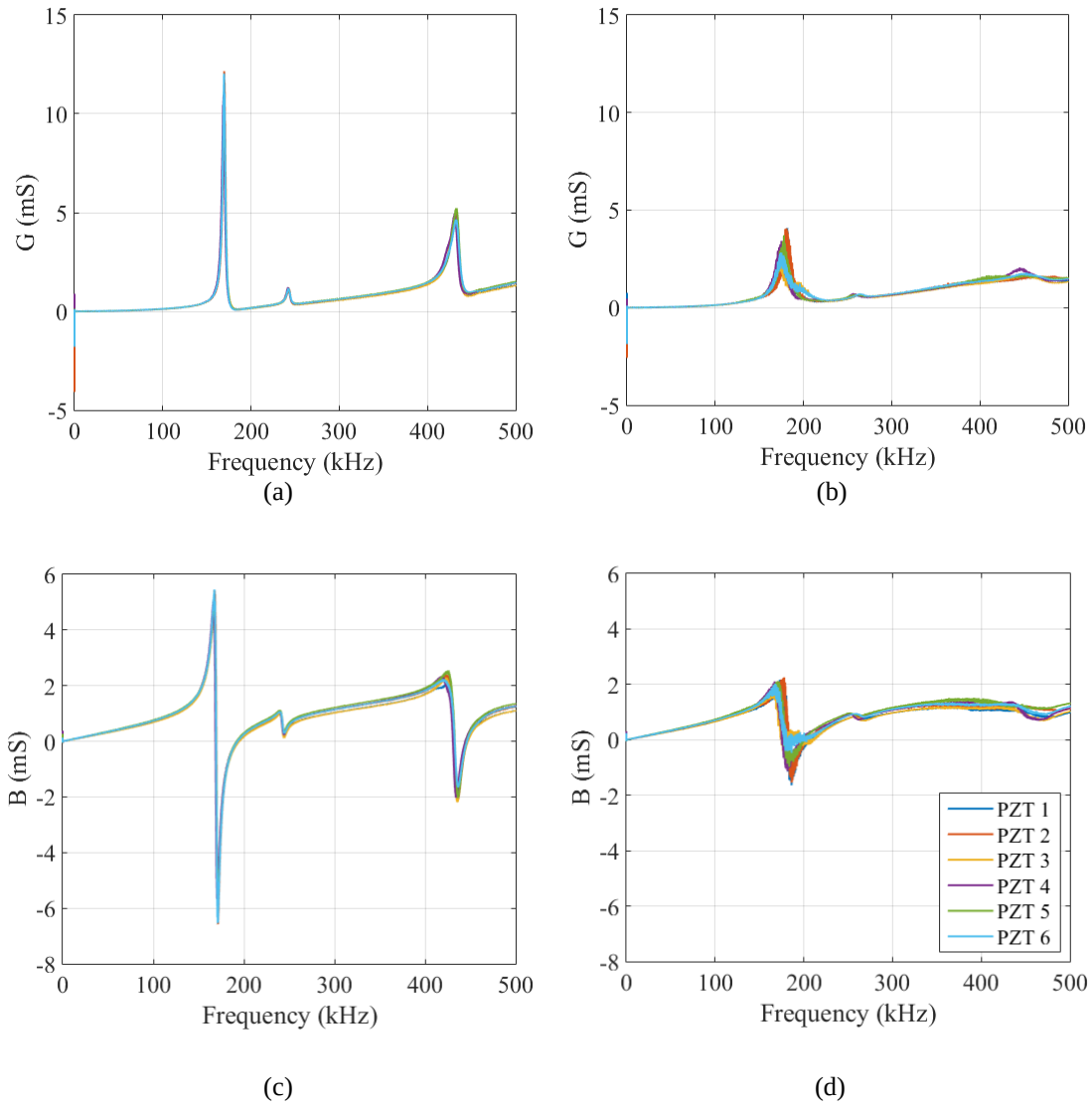

Figure 4.1 Conductance of (a) free PZT and (b) glued PZT to the pristine plate and susceptance of (c) free PZT and (d) glued PZT to the pristine plate

To quantify manufacturing difference, the RMSD of PZT 2 to 6 are calculated with respect to PZT 1. The results are presented in Table 4.2 and refer to the case prior and after bonding the PZTs to the plate. After the PZT are bonded, the RMSD value became higher, indicating the variability among the PZTs increased. This is due to slight variation in the bond line and the amount of epoxy used to bond the transducers to the plate.

The frequency range 91 – 94 kHz is considered throughout the study as Gulizzi et al. (2015). The conductance in this frequency range for the six free PZTs are all flat, thus, the peaks visible in the results represents the vibration modes of host structure and the bondline (Gulizzi, et al. 2015). This range is also far away from the PZT resonance frequencies, which guarantees the PZT impedance variation is not affected by the resonance of the transducer itself (Gulizzi, et al. 2015).

Table 4.1 RMSD of each PZT reference PZT 1 under the same pristine state

RMSD (100%)	PZT-1	PZT -2	PZT -3	PZT -4	PZT -5	PZT -6
Free PZT	0	2.03%	2.08%	2.77%	3.02%	3.73%
Bonded PZT	0	5.15%	2.47%	4.62%	6.54%	8.55%

4.2 GUWS MEASUREMENTS

Eight experiments are done for each transducer serving as actuator by manually connecting the actuator to the auxiliary circuit. These eight experiments include two consecutive measurements under pristine state without damage and six states with damage glued in six different locations. For illustrative purpose, only the signals for PZT 1 in pristine state are shown in Fig. 4.2.

In Fig. 4.2, the signal received by PZT1 is the output chirp signal after passing by the auxiliary circuit. Meanwhile, other 5 PZTs served as receivers and received the signal with the frequency range from 90 kHz to 210 kHz. Based on the impedance properties of the six transducers shown in Fig. 4.1, the resonance frequency is around 170 kHz, which

can be used for the signal reconstruction in the image processing analysis. This part of analysis is conducted by a collaborator and it is not presented in this thesis.

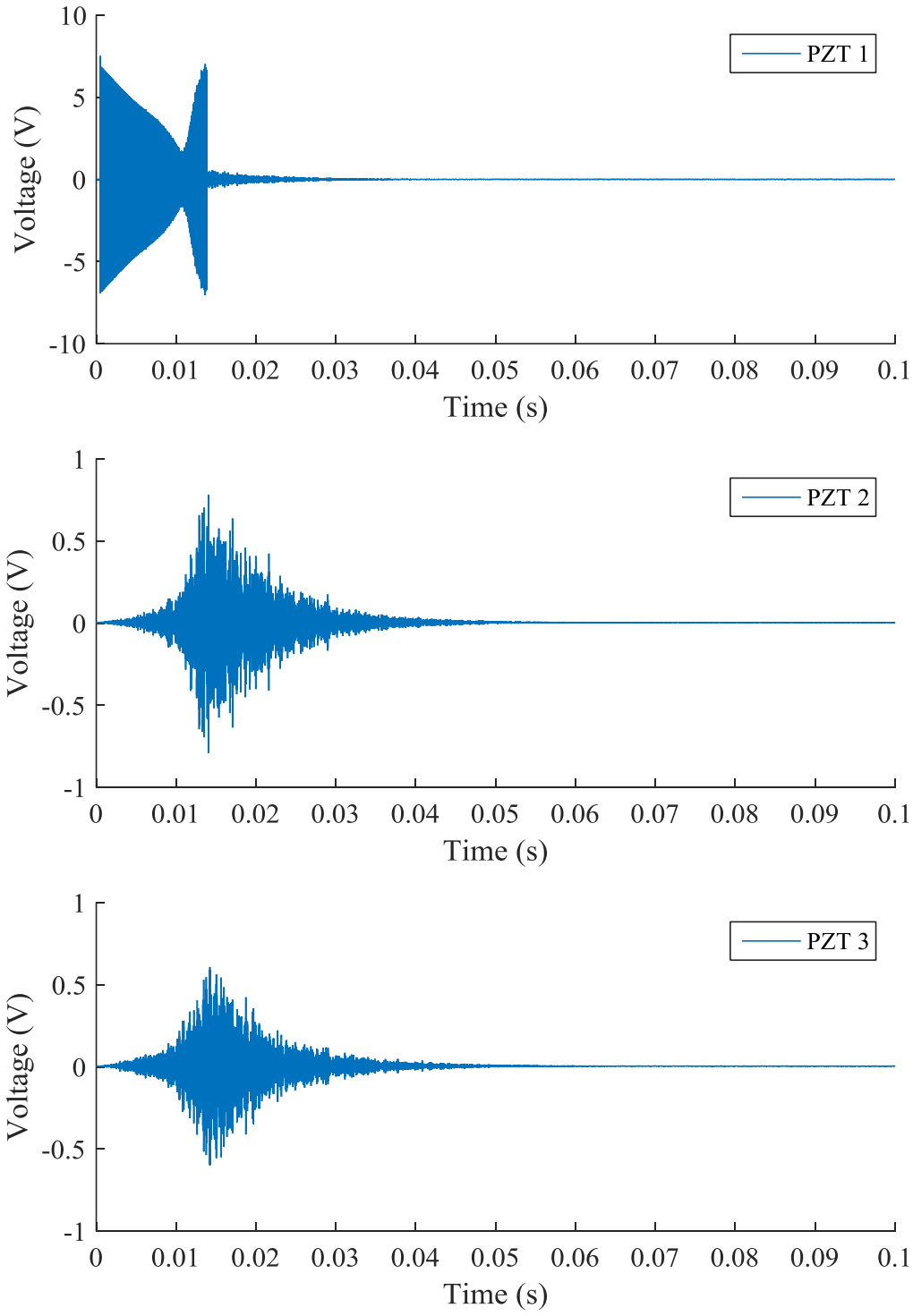

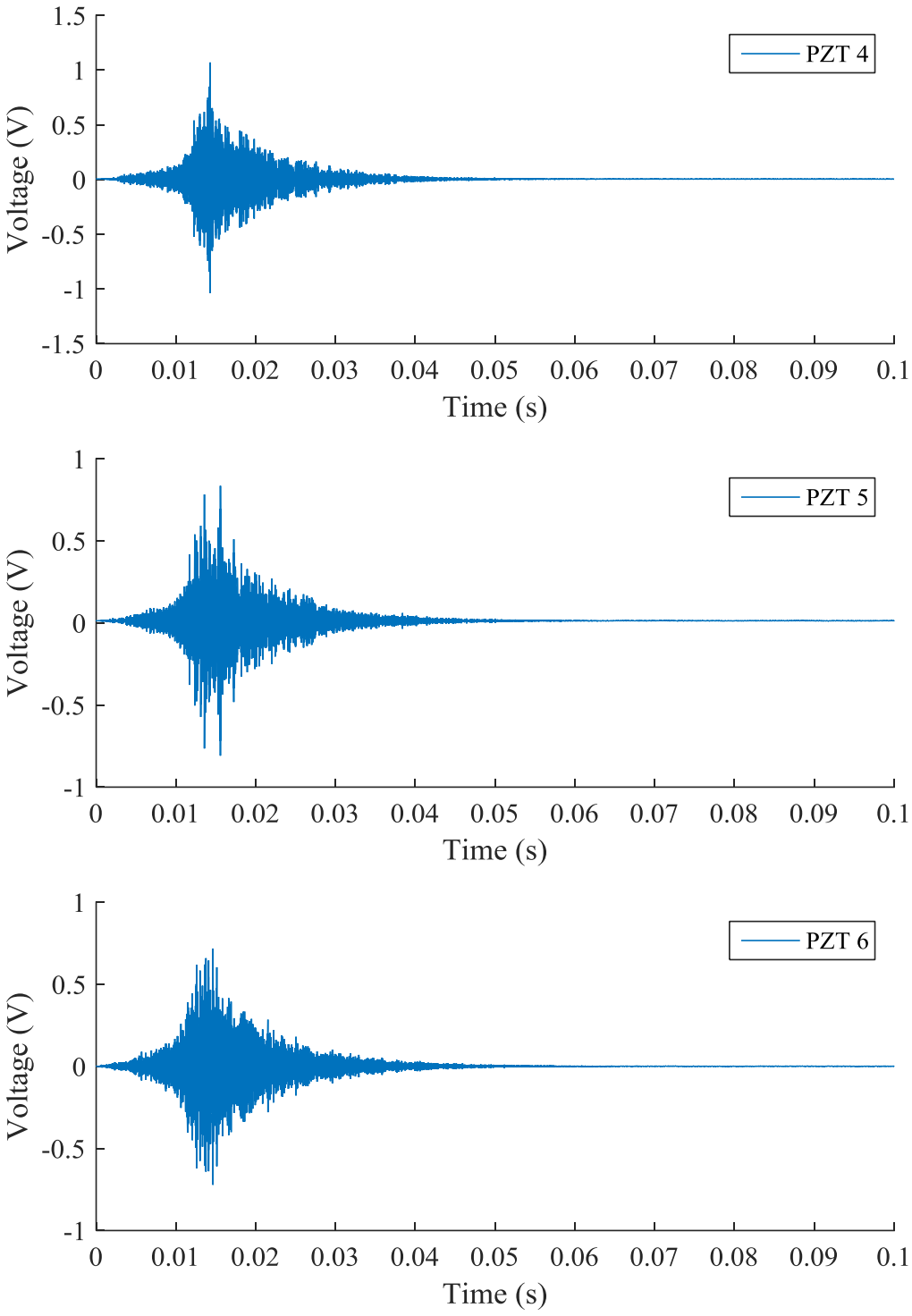

Figure 4.2 Actuation signal of PZT 1 and received signals of PZT 2-6

4.3 EMI MEASUREMENTS

4.3.1 Pristine State

Two measurements are conducted for the aluminum plate in pristine state using the integrated SHM system. Due to the amount of epoxy to bond the PZT and the electromechanical noise, the impedance signature may be slightly different between two measurements in the same state. Hence, a baseline, impedance variations of 6 PZTs between two measurements in pristine state, is considered in the observation.

For illustrative purposes, Fig. 4.3 shows the conductance in the 91 – 94 kHz frequency range associated with PZT 1 of two measurements under pristine state. There are some slight variations between these two measurements, however these variations are barely perceivable. Thus, four metric values between 2 pristine states are calculated using the Eq. (3.13a-d) in the frequency range 91 – 94 kHz as in ref. (Gulizzi, et al. 2015). The results are presented in Table 4.2 and set as baseline criteria.

For each damage metric, the metric value above the relative baseline criteria in Table 4.2 can be considered as an evidence of PZT impedance variation. For example, the RMSD value of the baseline is about 0.3% for all 6 PZTs. As such, a value of the RMSD value above 0.3% can be considered as an indicator of PZT impedance variation. Fig. 4.4 shows the signal waveforms of PZT 1 in the time domain for damage metric value calculation under one pristine state. The output chirp signal changed its shape after passing by the auxiliary circuit, indicating the impedance signature of the PZT.

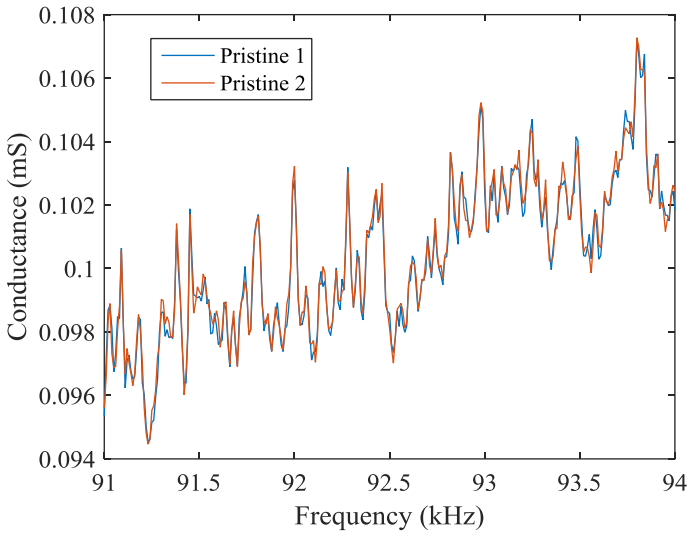

Figure 4.3 Conductance of (a) free PZT and (b) glued PZT to the pristine plate and susceptance of (c) free PZT and (d) glued PZT to the pristine plate.

Table 4.2 Baseline criteria of four damage metrics

	PZT1	PZT2	PZT3	PZT4	PZT5	PZT6
RMSD (%)	0.299855	0.256745	0.277376	0.26019	0.28225	0.322743
ASD	3.04E-11	2.31E-11	2.30E-11	2.25E-11	2.79E-11	7.19E-11
MAPD	0.727542	0.62607	0.666593	0.605197	0.686325	0.784447
M	2.72E-11	2.19E-11	2.25E-11	2.23E-11	2.72E-11	3.71E-11

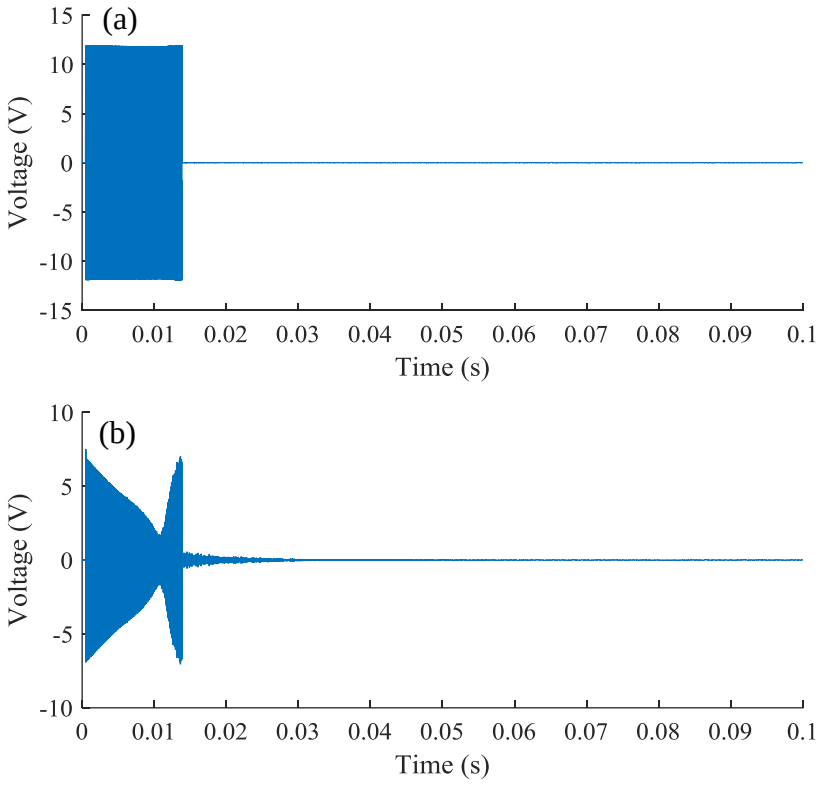

Figure 4.4 (a) Chirp signal excitation (b) EMI response of PZT 1 under pristine state

4.3.2 Damage State

The impedance signature of the six PZT actuators under the six damage states were measured. For illustrative purposes, Figure. 4.5 shows the conductance in the 91 – 94 kHz frequency range associated with the pristine case and the damage 6 scenario.

In Fig. 4.5(a), the peaks of the conductance reduce after adding the mass, indicating the impedance signature variation. The same trend is observed in Figs. 4.5(b) - (d) and Fig. 4.5(f). However, the variation between pristine and damage states were minimal. Figure 4.5(e) shows a remarkable difference between the pristine state and the damage 6 state, suggesting that damage 6 is close to PZT 5 and far away from other PZTs.

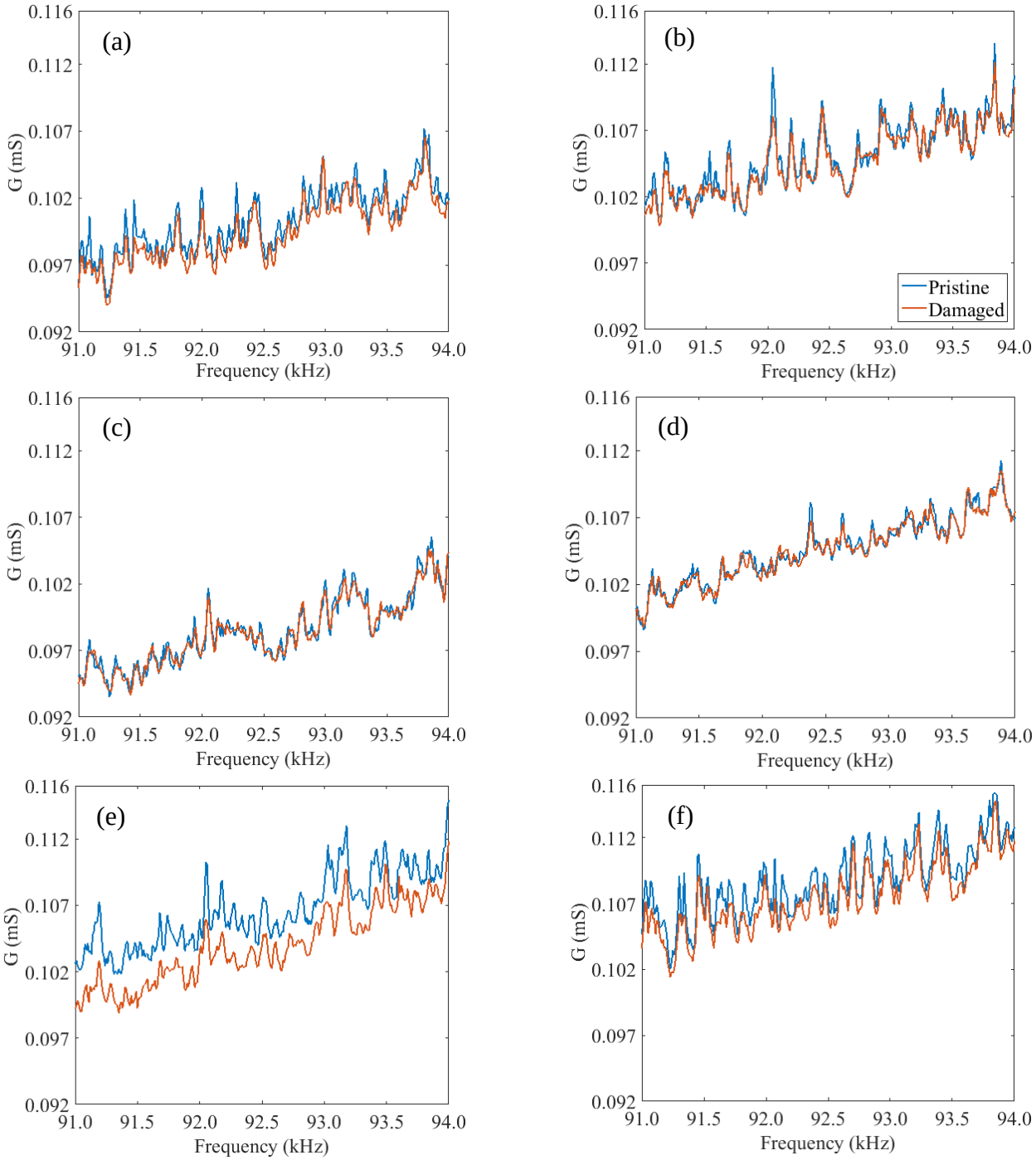

Figure 4.5 Comparison of the conductance of the (a) PZT 1, (b) PZT 2, (c) PZT 3, (d) PZT 4, (e)PZT 5 and (f) PZT 6 with that of the pristine plate when damage 6 is imposed

To observe the impedance signature variation more directly, the damage metrics were calculated. These metrics were calculated with respect to the pristine case. The histogram relative to the undamaged case refers to the two consecutive measurements obtained under pristine conditions. Ideally, the metrics relative to the same state should return a zero value. These metric value results are illustrated in Fig. 4.6 (a)-(d).

In Fig. 4.6, all the damage metric values follow the same trend that close damage corresponds to high metric value while far damage corresponds to low metric value. As such, in what follows, only the RMSD is discussed. For convenience, the value of the RMSD is presented as a function of the PZT (Fig 4.7) and as a function of the damage locations (Fig. 4.8), respectively.

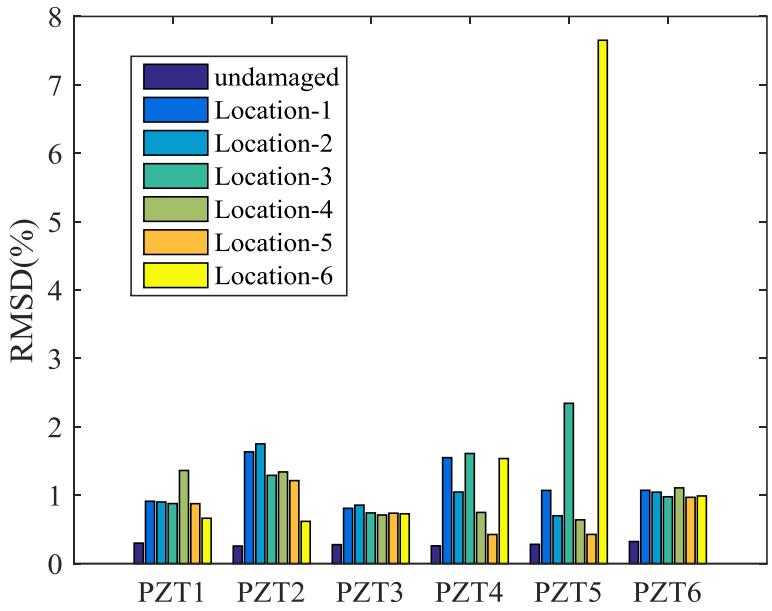
RMSD(%)
undamaged
Location-1
Location-2
Location-3
Location-4
Location-5
Location-6
PZT1
PZT2
PZT3
PZT4
PZT5
PZT6

(a)

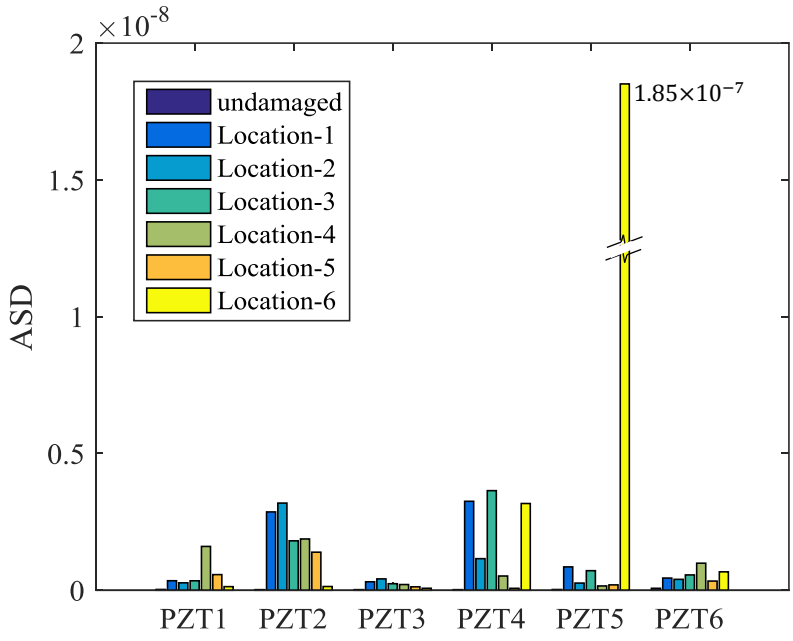
×10-8
ASD
undamaged
Location-1
Location-2
Location-3
Location-4
Location-5
Location-6
1.85×10−7
PZT1
PZT2
PZT3
PZT4
PZT5
PZT6

(b)

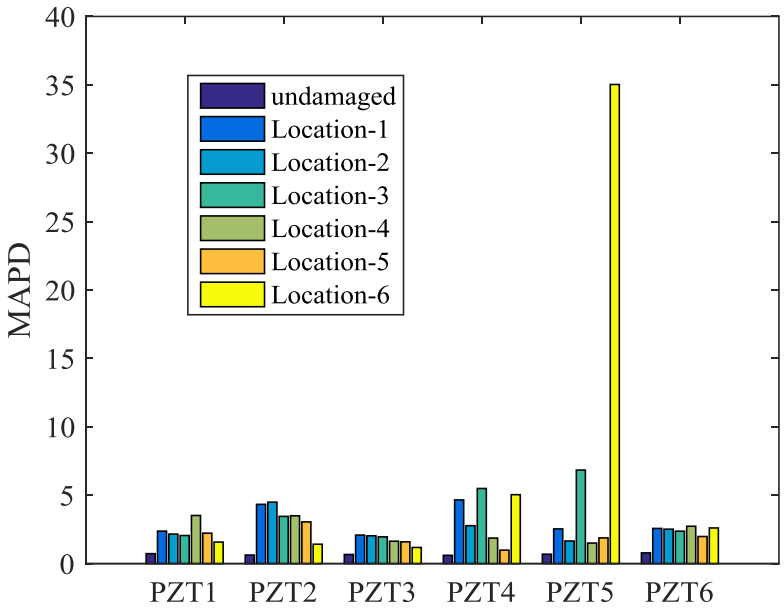

(c)

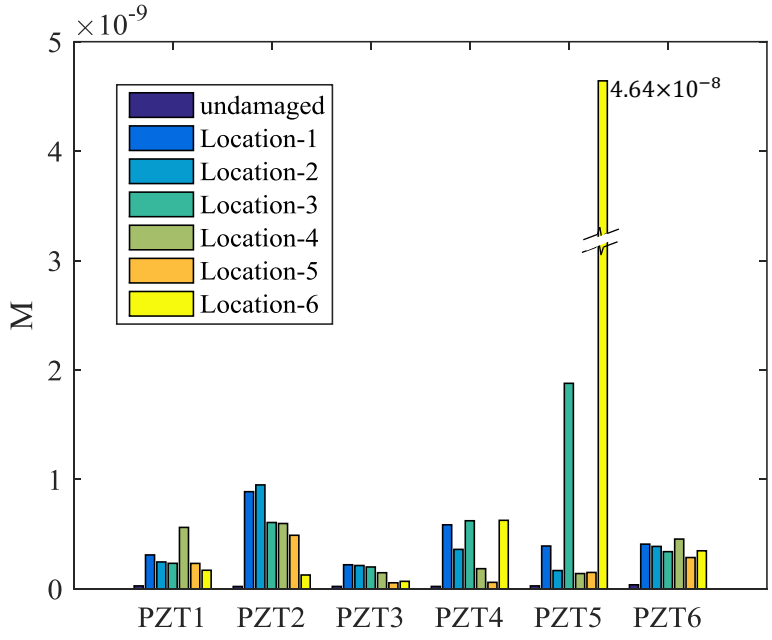

(d)

Figure 4.6 (a) RMSD (b) ASD (c) MAPD and (d) M values of the six PZTs in different damage location

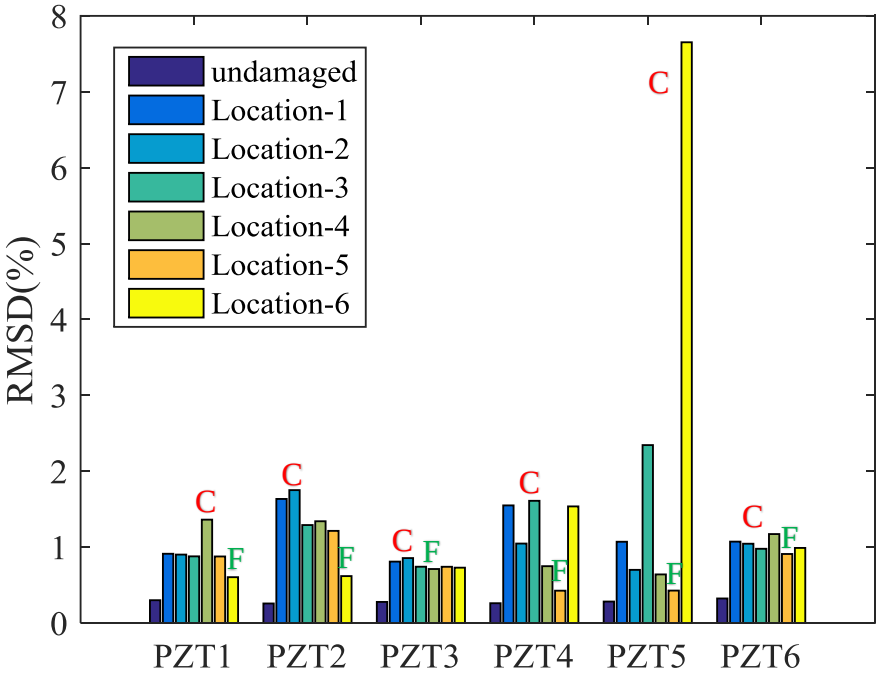

Figure 4.7 RMSD of different PZTs for all damage locations

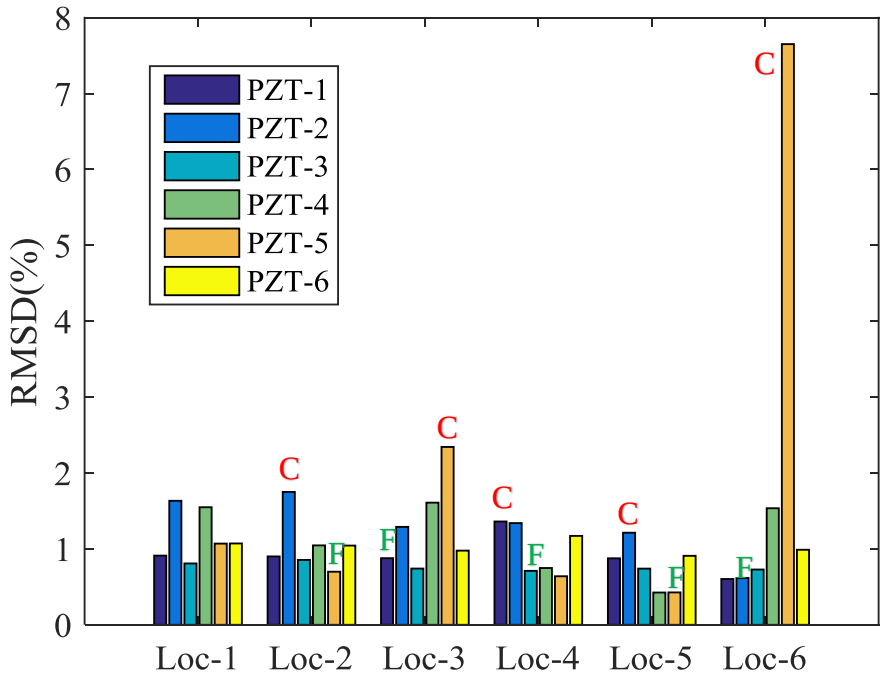

Figure 4.8 RMSD of different damage locations for all PZTs

In Fig. 4.7, all the RMSD values exceeded the baseline value of 0.3%, indicating the EMI method could detect damage. For each PZT, the highest RMSD correspond to the damage scenario, labeled as C in which the location of the damage was the closest to the PZT, while the lowest RMSD value correspond to the farthest damage location, marked as F. Thus, all six PZTs can detect the closest and furthest damage. As expected, the RMSD of PZT 5 and relative to damage 6 is remarkably high. The overall trend observed from the results is that the high RMSD value indicates that damage occurred in local area, while low RMSD value indicates that damage appeared in far field.

The data presented in Fig. 4.8 are clustered according to the damage location. Damage location 1 was at the centroid of the array but the RMSD were not identical for all PZTs. This is reasonable because the different performance of the six PZTs as shown in Table 4.3. However, for all other damage scenarios, the values of the RMSD identify properly which transducer was the closest and farthest from the added mass. This is emphasized with the labels C and F overlapped to the bars. According to the above results, using EMI method, the six PZTs could identify the presence of damage in local area.

Table 4.3 Distance from each damage location to each PZT (red-closet damage; green-farthest damage)

Distance	PZT-1	PZT -2	PZT -3	PZT -4	PZT -5	PZT -6
location-1	305	305	305	305	305	305
location-2	255	152	255	400	445	400
location-3	405	405	330	220	210	315
location-4	152	405	550	550	405	152
location-5	210	210	510	687	687	510
location-6	560	625	520	280	40	345

Note: The green cells denotes the closest PZT to the damage and the orange cells show the farthest one

5.0 CONCLUSIONS

In this study, a cost-effective integrated SHM system for conducting simultaneously GUWs and EMI analysis was investigated by using six PZT transducers bonded to an aluminum plate with added mass as simulated damage. This system consisted of one single hardware/software.

For each damage location, eight measurements were conducted: two involved pristine plate and six involved damage states. For each measurement, the GUWs and EMI data were obtained simultaneously. In this thesis, the analysis relative to the EMI data were presented. For these data, to quantify any variation of the impedance that may have resulted from the presence of damage, four damage metrics were employed, namely RMSD, ASD, MAPD and M.

The damage metric values obtained under damage states all exceeded the corresponding baseline, suggesting that the variation of the conductance enabled the detection of damage. The RMSD damage metric values regarding six PZTs with six damage locations were analyzed in detail. The metrics showed the trend that close damage corresponds to high metric value while far damage corresponds to low metric value.

It can be concluded that the damage location does affect the impedance signature variation and leads to different RMSD values. According to the RMSD of the six PZTs regarding the damage 6 scenario, the RMSD value was remarkably high as the damage was

significantly close to the PZT transducer, while it was considerably low when the damage was far away from the same PZT. This indicates that the PZT transducers can detect the local area around itself in the plate associated with a high damage metric value. For all damage locations 2-6, the highest RMSD value is detected by the closest PZT, while the lowest RMSD value is detected by the furthest PZT. This indicate that our system can detect the general damage location by showing a RMSD difference between the close and far damage. Thus, the six transducers employed in the presented system can be responsible for their local areas respectively, which can encompass a considerable area of the plate.

The detection results are different between these six transducers. One may assume that this is caused by the manufacturing difference between these six PZT transducers and the epoxy amount to glue these PZTs.

In summary, EMI method can show the damage in a circular neighborhood of the PZT, however, it is not able to locate the damage; thus, image processing, based on GUW results obtained from the same experiments can be employed to precisely localize the damages.

5.1 APPLICATION OF THE PRESENTED SHM SYSTEM

According to the conclusions, this integrated SHM system is able to obtain data for both GUWs and EMI analysis simultaneously. And the analysis results of EMI method demonstrate that, in an integrated SHM system, this method can be employed to encompass the local area around the PZT transducers bonded to the host structure.

For the existing structure, the PZT transducers are easy to bond on the surface of the structure. However, the wires fixation would be a considerable amount of work. As mentioned in section 5.2. The wireless PZT transducers can save a huge amount of work if it is proved reliable in the future. For the structures need to be constructed in the future, it is necessary to embed this integrated SHM system during construction process. Because it can save the long-term cost of inspection and maintenance, and it can also guarantee and even elongate the service life the structure.

5.2 FUTURE RESEARCH OF THE SHM SYSTEM

Since the damage in this study was simulated by gluing mass on the host structure, experiments with real damage should be conducted and relative experiment results should be observed. In this case, the damage metric value would be expected higher due to the bigger influence of the real damage to the host structure.

In addition, the eventual purpose of this integrated system is to cover the whole area of the host structure for inspection. Two methods including GUWs and EMI approach are incorporated in the presented system. In the future, acoustic emission (AE) could be incorporated in this system. AE can record the real-time damage development. In this system, the bonded PZT transducers can be used to listen to the structure when they are available from other two methods. This should be achieved and incorporated in the current LabVIEW program.

Moreover, for the EMI analysis, the temperature change plays an important role for the impedance variation (Wandowski, et, al. 2016). In this thesis, the temperature

compensation was not considered since the temperature in the lab could be considered constant. In real applications, the variation of temperature may be considerably high due to the environmental factors (Park et, al. 1999). This can change the boundary conditions and affect the mechanical impedance property of the structure. The research related to the influence of temperature for the impedance signature need to be conducted to obtain better temperature compensation.

For the monitoring of large structures, a relevant huge SHM system is needed. In this case, the wires to connect the sensors and detection equipment would be numberless. The fixation work would also be tedious and costly. Thus, the reliable wireless sensors should be developed and put into practice in the SHM system (Haque, et, al. 2015).

In the research, the actuator need to be changed manually. A switch box is used at the preliminary design of the experiment setup to make the actuator change automatically. Later, in the experiments, this equipment introduces a low frequency noise, which has a significant influence on the expected results. We tried filters to remove this noise, but the expected signal changes significantly. Thus, the switch is not used in the final experiments. In the future, switch box without introducing considerable noise should be used to make this system change actuator automatically.

BIBLIOGRAPHY

An, Y.K., & Sohn, H. "Integrated impedance and guided wave based damage detection under temperature variation." *SPIE Smart Structures and Materials+ Nondestructive Evaluation and Health Monitoring, 12*, 79811Q-79811Q, 2011.

An, Y. K., Kim, M. K., & Sohn, H. "Airplane hot spot monitoring using integrated impedance and guided wave measurements." *Structural Control and Health Monitoring, 19*(7), 592-604, 2012.

Baptista, F. G., Vieira Filho, J., & Inman, D. J. "Sizing PZT transducers in impedance-based structural health monitoring." *IEEE Sensors Journal, 11*(6), 1405-1414, 2011.

Bhalla, S., Gupta, A., Bansal, S., & Garg, T. "Ultra low-cost adaptations of electro-mechanical impedance technique for structural health monitoring." *Journal of Intelligent Material Systems and Structures, 00*, 1-10, 2009.

Bhalla, S., & Soh, C. K. "Electromechanical impedance modeling for adhesively bonded piezo-transducers." *Journal of Intelligent Material Systems and Structures, 15*(12), 955-972, 2004.

Giurgiutiu, V., Reynolds, A., & Rogers, C. A. "Experimental investigation of E/M impedance health monitoring for spot-welded structural joints." *Journal of Intelligent Material Systems and Structures, 10*(10), 802-812, 1999.

Gresil, M., & Giurgiutiu, V. "Electromechanical Impedance Spectroscopy and Guided Wave Propagation Predictive Modeling on Composite Materials." *Paper presented at the EWSHM-7th European Workshop on Structural Health Monitoring, 17*(9), 1825-1832, 2014.

Gresil, M., Yu, L., Giurgiutiu, V., & Sutton, M. "Predictive modeling of electromechanical impedance spectroscopy for composite materials." *Structural Health Monitoring, 11*(6), 671-683, 2012.

Gulizzi, V., Rizzo, P., & Milazzo, A. "On the Repeatability of Electromechanical Impedance for Monitoring of Bonded Joints." *AIAA Journal, 53*(11), 3479-3483, 2015.

Gulizzi, V., Rizzo, P., Milazzo, A., & Ribolla, E. L. M. "An integrated structural health monitoring system based on electromechanical impedance and guided ultrasonic waves." *Journal of Civil Structural Health Monitoring*, *5*(3), 337-352, 2015.

Haque, M. E., Zain, M. F., Hannan, M. A., & Rahman, M. H. "Building structural health monitoring using dense and sparse topology wireless sensor network." *Smart Structures and Systems*, *16*(4), 607-621, 2015.

Kettle, R. A., and Anton S. R. "Rapid evaluation of mechanical boundary conditions using impedance based structural health monitoring." *SPIE Smart Structures and Materials+ Nondestructive Evaluation and Health Monitoring*, *13*, 98051S-98051S, 2016.

Koo, K.Y., Park, S., Lee, J.-J., & Yun, C.-B. "Automated impedance-based structural health monitoring incorporating effective frequency shift for compensating temperature effects." *Journal of Intelligent Material Systems and Structures*, *00*, 1-12, 2008.

Liang, C., Sun, F., & Rogers, C. "Coupled electro-mechanical analysis of adaptive material systems—determination of the actuator power consumption and system energy transfer." *Journal of Intelligent Material Systems and Structures*, *5*(1), 12-20, 1994.

Wandowski, T., Malinowski, P. H., & Ostachowicz, W. M. "Delamination detection in CFRP panels using EMI method with temperature compensation." *Composite Structures*, *151*, 99-107, 2016.

Maruo, I. I. C., de Faria Giachero, G., Junior, V. S., & Neto, R. M. F. "Electromechanical Impedance-Based Structural Health Monitoring Instrumentation System Applied to Aircraft Structures and Employing a Multiplexed Sensor Array." *Journal of Aerospace Technology and Management*, *7(3)*, 294-306, 2015.

Na, W. S., & Park, K.-T. "A cost-effective impedance-based structural health monitoring technique for steel structures by monitoring multiple areas." *Journal of Intelligent Material Systems and Structures*, 1045389-16645866, 2016.

Panigrahi, R., Bhalla, S., & Gupta, A. "A low-cost variant of electro-mechanical impedance (EMI) techinique for structural health monitoring." *Experimental Techniques*, *34*(2), 25-29, 2010.

Park, G., Kabeya, K., Cudney, H. H., & Inman, D. J. "Impedance-based structural health monitoring for temperature varying applications." *JSME International Journal Series A Solid Mechanics and Material Engineering*, 42(2), 249-258, 1999.

Park, G., Cudney, H. H., & Inman, D. J. "Impedance-based health monitoring of civil structural components." *Journal of infrastructure systems*, *6*(4), 153-160, 2000.

Park, G., Cudney, H. H., & Inman, D. J. "Feasibility of using impedance-based damage assessment for pipeline structures." *Earthquake engineering & structural dynamics, 30*(10), 1463-1474, 2001.

Park, G., & Inman, D. J. "Structural health monitoring using piezoelectric impedance measurements." *Philosophical Transactions of the Royal Society of London A: Mathematical, Physical and Engineering Sciences, 365*(1851), 373-392, 2007.

Park, G., Sohn, H., Farrar, C. R., & Inman, D. J. "Overview of piezoelectric impedance-based health monitoring and path forward." *Shock Vib. Dig. 35*, 451–63,2003.

Park, S., Lee, J.-J., Yun, C.-B., & Inman, D. J. "Electro-mechanical impedance-based wireless structural health monitoring using PCA-data compression and k-means clustering algorithms." *Journal of Intelligent Material Systems and Structures*, 19(4), 509-520, 2007.

Peairs, D. M. "Development of a Self-Sensing and Self-Healing Bolted Joint." Dissertation, Virginia Polytechnic Institute and State University, 2002.

Peairs, D. M., Park, G., & Inman, D. J. "Improving accessibility of the impedance-based structural health monitoring method." *Journal of Intelligent Material Systems and Structures, 15*(2), 129-139, 2004.

Pohl, J., Herold, S., Mook, G., & Michel, F. "Damage detection in smart CFRP composites using impedance spectroscopy." *Smart materials and structures, 10*(4), 834, 2001.

Raju, V. "Implementing Impedance – Based Health Monitoring." Dissertation, Virginia Polytechnic Institute and State University, Virginia, 224p, 1997.

Tseng, K. K-H. and Naidu, A. S. K. "Non-parametric damage detection and characterization using smart piezoceramic material." *Journal Smart Material and Structures. 11*, 317-329, 2002.

Wang, D., Song, H., & Zhu, H. "Electromechanical Impedance Analysis on Piezoelectric Smart Beam with a Crack Based on Spectral Element Method." *Mathematical Problems in Engineering, 13*, 81-94, 2015.

Xu, B., & Giurgiutiu, V. "A low-cost and field portable electromechanical (E/M) impedance analyzer for active structural health monitoring." *Proceedings of the 5th International Workshop on Structural Health Monitoring Stanford*, 634–644, 2005.

Zagrai, A. N., & Giurgiutiu, V. "Electro-mechanical impedance method for crack detection in thin plates." *Journal of Intelligent Material Systems and Structures, 12*(10), 709-718, 2001.

Zhu, X., & Rizzo, P. "A unified approach for the structural health monitoring of waveguides." *Structural Health Monitoring*, *11*(6), 629-642, 2012.